BOUNDARY CORRECTIONS FOR A THREE-COIL CONDUCTIVITY/VELOCITY PLASMA PROBE

BY

EDWARD W. VENDELL

Bachelor of Science in Mechanical Engineering
University of Utah
Salt Lake City, Utah
1955

Master of Science in Mathematics
University of Utah
Salt Lake City, Utah
1960

Submitted to the faculty of the Graduate College
of the Oklahoma State University
in partial fulfillment of the requirements
for the degree of
DOCTOR OF PHILOSOPHY
May, 1967

BOUNDARY CORRECTIONS FOR A THREE-COIL

CONDUCTIVITY/VELOCITY PLASMA PROBE

Thesis Approved:

Donald R. Hawsth
Thesis Adviser

Vernon J. Rossow

J. A. Wiebelt

J. G. Trump

D. D. Durham
Dean of the Graduate College

ACKNOWLEDGMENTS

The author is deeply indebted to Dr. Vernon J. Rossow for the privilege and experience of working with him at the Ames Research Center, Moffett Field, California. He was a continual source of inspiration and guidance during the preparation of this report. Grateful acknowledgment is also made to Dr. Rossow and Mr. Rudolph E. Posch for their permission to use selected material from their paper. The author also wishes to thank Mr. Posch for many helpful insights and suggestions.

LIST OF PRINCIPAL SYMBOLS

$\underset{\sim}{A}$	vector potential function
$\underset{\sim}{B}$	magnetic induction vector
$\underset{\sim}{B}_p$	primary dipole magnetic induction vector
$\underset{\sim}{b}_t, \underset{\sim}{b}_{\|\|}$	first-order magnetic induction vectors
$\underset{\sim}{D}$	electric displacement vector
$\underset{\sim}{E}$	electric field intensity vector
e	electron charge
$\underset{\sim}{H}$	magnetic field intensity vector
I_p	total current, primary coil
$\underset{\sim}{J}$	current density vector
$\underset{\sim}{J}_t, \underset{\sim}{J}_{\|\|}$	first-order current density vectors
m_e	mass of an electron
m_A	mass of an atom
n_e	electron number density
n_I	ion number density
n_p	number of turns, primary coil
n_Σ	number of turns, Σ coil
n_Y	number of turns, Y coil
Q_o	quality factor of an electric circuit
Q_{eA}	electron-atom collision cross section
R	radius of a cylindrical region
R_m	magnetic Reynolds number

r	distance in spherical coordinates
r_p	characteristic radius, primary coil
r_Σ	characteristic radius, Σ coil
r_Y	characteristic radius, Y coil
T	temperature
t	subscript refers to first-order fields caused by σ
$\underset{\sim}{U}$	velocity vector
$U_{\|\|}$	axial velocity component
X,Y,Z	dimensionless Cartesian coordinates
x,y,z	Cartesian coordinates
y_Σ	distance from primary coil to either secondary coil
z	axial coordinate
α	degree of ionization
δ	magnetic skin depth factor
ϵ	dielectric constant
Θ_Σ	boundary correction factor for σ
Θ_Y	boundary correction factor for $\sigma U_{\|\|}$
θ	azimuthal coordinate
μ	magnetic permeability
$\bar{\nu}_e$	average electron collision frequency
ρ	radial coordinate
Σ	conductivity coil
σ	electrical conductivity
Y	conductivity-velocity coil
Φ_Σ	signal induced on Σ coil
$\Phi_{\Sigma\infty}$	signal induced on Σ coil in an infinite medium
Φ_Y	signal induced on Y coil

Φ_Y	signal induced on Y coil in an infinite medium
ψ	stream function for current density
ω	frequency of impressed power
ω_p	plasma electron frequency
$\parallel$	subscript refers to first-order fields caused by $\sigma U_{\parallel}$

SUMMARY

A three-coil plasma probe that measures both the conductivity and velocity of laboratory plasmas having low magnetic Reynolds numbers has been developed and tested by Rossow and Posch. As a first approximation, it was assumed that the plasma boundary was far from and much larger than the probe. At the suggestion of V. J. Rossow, the present work was undertaken to extend the previous theory by deriving factors which correct for the presence of cylindrical boundaries. As a check on this numerical work, several computed values were compared with experimental data taken in cylinders of acid. Since the agreement was satisfactory, the boundary correction factors were used to reduce data taken as the probe was swept through an argon plasma generated by a constricted-arc wind tunnel. These resultant profiles represent local values of the conductivity and velocity in the presence of the boundary of the plasma jet that are in agreement with estimates made by other means. It was found that the raw data underestimates conductivity and overestimates velocity.

TABLE OF CONTENTS

CHAPTER I

INTRODUCTION

A plasma is an ionized, electrically-conducting gas consisting, in the general case, of electrons, positive or negative ions, atoms, molecules, and photons; most definitions add the restriction that a plasma must be electrically neutral on a macroscopic scale. The non-neutral particles may be multiply ionized and the neutrals (atoms or molecules) may be electronically excited. The photons may exhibit a broad spectrum of quantized frequencies. Plasma temperatures can range from 100° K in interstellar space to more than 10^{8} $^{\circ}$K in a thermonuclear reaction. However, the present work is primarily concerned with laboratory plasmas which are generated by electric arcs and have temperatures from 5000° K to $40{,}000^{\circ}$ K. Perhaps the most important characteristic of a plasma is its ability to conduct an electric current; this fact accounts for the existence of the many and diverse phenomena that have been observed in ionized gases.

The transport properties of a plasma differ markedly from those of an un-ionized gas because the Coulomb-type interparticle forces existing in the former are vastly different from the nonelectrical interparticle forces in the latter. The measurement of these properties in high temperature laboratory plasmas has necessitated the modification of traditional transducers, such as pitot tubes and thermocouples, to withstand high heat flux rates and function properly in an ionized environment

without greatly perturbing the medium. In addition, it has been necessary to develop measurement techniques to determine electron and ion temperatures (which are not equal in a nonequilibrium plasma), particle number densities, and the total electron collision frequency. Some measurements are made externally be means of X-ray, microwave, and laser interferometry and absorption or emission spectroscopy. The properties may then be used to infer the transport coefficients by means of an appropriate formula.

However, internal measurements are desirable to serve as a check on the external data and to obtain, if possible, local values. For example, in the design of magnetohydrodynamic power generators and accelerators, knowledge of local conductivity and velocity is of vital importance in choosing electrode locations and in determining efficiency. But the hostile plasma environment poses severe design problems. Consequently, many conductivity instruments have been designed (see, for example, Reference 1-15, 20) but only a few are immersible (see References 4, 5, and 20). In Chapter II a representative sampling of previous conductivity and velocity measurement techniques are reviewed.

The present work is based on a design by Rossow and Posch (20) of an immersible three-coil conductivity/velocity probe which represents a significant improvement upon previous methods because it minimizes the heat flux sensitivity (4, 5) and large flow perturbation (4) problems of other designs. Briefly, this instrument consists of a primary and two secondary coils. The alternating current in the primary coil creates an oscillating magnetic dipole field. The secondary coils are located in such a manner as to respond to perturbations of the pri-

mary dipole field caused by the electrical conductivity and the motion of the surrounding medium. Further details of this instrument are presented in Chapter II.

In the theoretical analysis of most magnetofluidmechanic problems, the magnetic Reynolds number, $R_m = \sigma\mu U l$, indicates the relative magnitudes between the impressed and induced magnetic fields. In this definition σ is the electrical conductivity, μ is the permeability, U is the speed, and l is some characteristic length. If R_m is small, Reference 21 shows that the induced magnetic field is also small compared to the impressed field. Then the analysis can be greatly simplified by the use of a power series expansion in R_m since only first-order terms need be considered. This approach was used in the analysis of Rossow and Posch because R_m is small for most plasmas generated by electric arcs; the probe design of Reference 20 was tested in a constricted-arc wind tunnel where R_m ranged from 10^{-4} to 10^{-1}. Therefore, the neglect of terms of order R_m^2 was reasonable.

The theory of Rossow and Posch also assumed an unbounded plasma having uniform electrical conductivity and velocity. The principal purpose of the present work is to present theoretical modifications which will remove these restrictions for the case of a free plasma jet having a cylindrical boundary.

Accordingly, Chapter III presents modifications of the unbounded field theory which are necessary whenever the three-coil probe nears a plasma boundary. Initially, the conductivity σ and velocity $\underset{\sim}{U}$ are assumed to be constant inside the jet of radius R and zero elsewhere as illustrated in Figure 1. Using this idealized model, the modifications are derived and presented graphically in the form of boundary

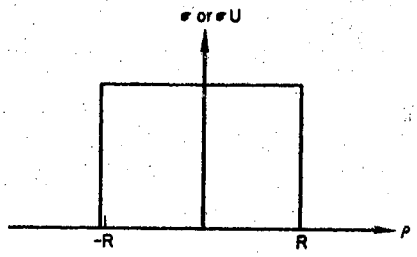

Figure 1. Cross-stream variation of plasma variables assumed in theory.

correction factors. These theoretical correction factors are compared with experimental results obtained by the probe in a deep plastic cylinder filled with an electrolyte.

In Chapter IV the correction factors are utilized to develop a method for computing the local conductivity and velocity of a plasma stream from data (similar to that of Figure 2) which varied continously

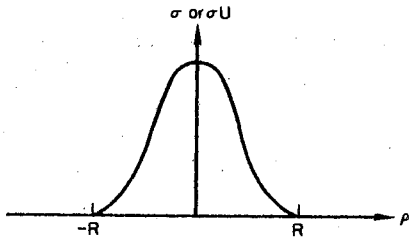

Figure 2. Typical profile in plasma jet.

across the stream as obtained by a probe as it was swept through an argon plasma jet generated by a constricted-arc wind tunnel. The method is then applied to a typical data record and the resulting conductivity and velocity profiles are presented and discussed.

Chapter V contains concluding remarks, and the Appendix includes a discussion of electrical conductivity formulas, computer program details, and remarks on displacement currents in plasmas and electrolytes.

CHAPTER II

PREVIOUS INVESTIGATIONS

In the first section of this chapter, several representative conductivity measurement techniques are reviewed (References 1-15). Velocity measurement devices are discussed in the second section (References 16-19). A third section is devoted to a review of the conductivity/velocity probe system designed by Rossow and Posch (20).

Electrical Conductivity

Many electrical conductors obey a very simple relationship, known as Ohm's law, involving the current density vector $\underset{\sim}{J}$, the electrical conductivity σ, and the applied electric field intensity vector $\underset{\sim}{E}$. This familiar equation is

$$\underset{\sim}{J} = \sigma \underset{\sim}{E} \tag{1}$$

where σ is a property of the conductor.

At first glance it is tempting to extend this law to plasmas and to measure σ by inserting two electrodes into the ionized gas and then observe the current which results from the application of a known electric field. However, the introduction of such a device, called a Langmuir probe, into a plasma results in various boundary layer and electrode surface effects which can greatly influence the measured resistance. Therefore, Langmuir probes are seldom used to determine

σ. However, a theory has been developed to utilize the Langmuir probe for the measurement of ion number density and ion and electron temperatures.

The ideal immersible plasma conductivity probe has many design requirements. If the probe is used in a plasma jet from an arc discharge, then it must withstand high heat flux rates. The probe output should not be significantly affected by the electric charge sheath or the thermal and velocity boundary layers which form on it surfaces. If the probe is supplied with pulsating power, then the impressed frequency ω must be much less than ν_e, the average electron collision frequency. This restriction assures that electrons will suffer many collisions per cycle and, consequently, that the effective dc conductivity will be measured. Also, the impressed frequency must avoid resonance effects with the electron plasma frequency

$$\omega_p^2 = n_e e^2/m_e \varepsilon_o \tag{2}$$

where e is the electron charge, n_e is the electron particle density, ε_o is the permittivity of free space, and m_e is the electron mass. Equation (2) represents the frequency of electrostatic electron oscillations that may occur in a plasma as a result of microscopic charge separation, ω_p for laboratory plasmas is of the order 10^{12}Hz. Another restriction on the magnitude of ω is related to the electromagnetic skin depth factor δ defined by the relationship

$$\delta = (2/\sigma\omega\mu)^{\frac{1}{2}} \tag{3}$$

where μ is magnetic permeability, δ is a measure of the depth of penetration of an electromagnetic field into a conducting medium. The magnitude of ω must be chosen so that the probe's magnetic field

penetrates beyond the adjacent conducting boundary layers into the unperturbed free stream. However, in direct opposition to these limitations on the maximum value of ω, the impressed frequency must be great enough to ensure an acceptable signal-to-noise ratio. Calibration should be simple, convenient, and accurate. A linear relationship between output signal and conductivity is preferred. Finally, the device should not be too costly or complicated.

Many electrical conductivity measurements utilize a solenoid that is external to and coaxial with a cylindrical plasma stream or a shock tube (see, for example, Reference 1-3, 6-15). If the solenoid is supplied with a small amount of power to generate a "primary" magnetic field within the core, then "secondary" search coils may be used to sense the perturbation of the primary field caused by the presence and/or motion of a conducting core. The voltages induced on the secondaries are then used to infer the conductivity or velocity of the coaxial medium. When the primary power supply is constant (1), the conducting medium must be in motion; this restriction may be removed by the use of pulsating power (11-14), subject to the limitations on the impressed frequency mentioned above.

Alternately, the coaxial solenoid may be used as an active component of a tuned, oscillating, L-C network. The introduction of a conducting medium into the core of the solenoid causes a change, Δf, in the resonant frequency, f_o, of the circuit and a change, ΔQ, in the quality factor, Q_o, of the circuit. The quality factor, Q, is defined as the ratio of the time averaged energy stored in the oscillator

circuit to the energy loss per cycle. Calibration curves are used to predict conductivity as a function of $\Delta f/f_o$ (8-10) or as a function of $\Delta Q/Q_o$ (7).

Another technique employs two identical single-layer solenoids as the active elements of a symmetrical RF bridge. The bridge is balanced when air is the core medium in both coils. Introduction of a plasma into the core of one solenoid causes the bridge to become unbalanced and the magnitude of the unbalance may be related to the average conductivity of the plasma core. The bridge power may be sinusoidal (3) or pulsed (2).

The method of Luther (11) employs a long, coaxial solenoid and a small one-turn coil that is inserted into the plasma core through a hole in the solenoid. The search coil is used to determine a radial profile of the axial magnetic field B_z. Then $U_{||}$ is related to B_z and its radial gradient, $\partial B_z/\partial \rho$, by means of a theoretical analysis.

As previously mentioned, few immersible probes have been reported. The device of Olson and Lary (4) consists of a small (8mm o.d.) cylindrical single-layer solenoid enclosed in an insulating tube. The sinusoidal power which is supplied to the coil induces plasma currents. The power dissipated by these currents may be measured and related to the average electrical conductivity. The recent design by Stubbe (5) is similar to that of Olson and Lary and uses a much smaller coil (1.4 mm o. d.). The three-coil conductivity/velocity probe of Rossow and Posch (20) is described below in a separate section of this chapter.

Each of the methods discussed above suffers from one or more disadvantages. The technique of Lin et al. (1) employs a coaxial primary solenoid supplied with constant power and a single upstream secondary

or sensing coil. Although this method is comparatively uncomplicated, it is limited to moving gases and cannot be used to obtain local values of σ. Fuhs (12) has improved the Lin configuration by adding a downstream secondary coil and changing the primary power supply to sinusoidal ($\omega = 800\pi$ Hz). These revisions remove the restriction on moving gases and permit the calculation of a σU profile where $U_{\parallel}$ is the axial velocity; however, the method does not yield separate σ and $U_{\parallel}$ profiles.

The two-solenoid, pulse-operated bridge method of Persson (2) relates the bridge unbalance caused by the plasma core to a radial average of the ratio $n_e/\bar{\nu}_e$. Conductivity is then computed by means of the formula

$$\sigma = (n_e/\bar{\nu}_e)(e^2/m_e). \tag{4}$$

The use of this formula is a disadvantage because this equation involves many assumptions, some of which are discussed in Appendix A. Koritz and Keck (3) used a bridge supplied with sinusoidal power (ω = 3.8 MHz) and related bridge unbalance directly to a radial average value of σ. The principal disadvantage of these two bridge techniques is their inability to determine local values.

The devices reported by Blackman (6), Donskoi et al. (7), Akimov and Konenko (8), Tanaka and Hagi (9), and Savic and Boult (10) are based on the $\Delta f/f_o$ method outlined above.

Akimov and Konenko (7) have pointed out two potential sources for error in the $\Delta f/f_o$ and $\Delta Q/Q_o$ methods. 1. Because the stray capacitance of a coil is increased in the vicinity of a conductor, the L-C network must be designed so that the stray capacitance problems encountered by Tanake and Hagi will be negligible. 2. To obtain acceptable

sensitivity, the $\Delta f/f_o$ method must use frequencies of the order 1 MHz to 50 MHz. Because all plasma jets are radially nonuniform, the electromagnetic skin depth factor ζ, being inversely proportional to σ, increases from a minimum at the center of the jet to a maximum at the edge of the jet. Therefore, it is possible that the use of a high frequency power supply may prevent adequate penetration of the applied field into the highly conductive core of a plasma jet so that the change, Δf, may not be proportional to a radial average of the conductivity. Akimov and Konenko suggest that ζ/R must exceed 1.6 at the center of the plasma jet and this requirement caused Akimov and Konenko to question the results of Blackman's experiments.

Several investigators have objected to calibration methods which employ electrolytes because the displacement current may not be negligible in a polarizable electrolyte at the high frequencies employed for the $\Delta f/f_o$ techniques (see Appendix C for a discussion on the displacement current). Therefore, Savic and Boult used mercury, copper, and a bizmuth-tin alloy for calibration materials. However, the resulting calibration curve was nonlinear and did not extend below 700 mho/meter.

The method of Tanaka and Hagi is based on the existence of an annular gap between the coil and the plasma core and the theory shows that this instrument may be calibrated using an air core. The techniques of Hollister (15) and Donskoi et al (7) are similar to that of Tanaka and Hagi. Poberezhskii (13), commenting on the work of Donskoi et al., has shown that a small error in the ratio of the jet radius to the coil radius can result in a large conductivity error. This could be a serious disadvantage because in many instances it is difficult to determine the radius of the jet.

The instrument of Poberezhskii (14) is similar to the Fuhs device except that this design employs one primary and four secondary coils which coaxially surround the plasma jet. The theory indicates that if two secondary coils, symmetrically located with respect to the primary, are wound in the same direction, then the potential induced on those two coils will be proportional to σ. Similarly, the potential induced on the remaining two coils, wound in opposition, will be proportional to σU . However, the technique employs complicated circuitry, yields only average values, and is sensitive to extraneous signals.

With one exception, none of the external solenoid devices is capable of obtaining a local value of σ. Poberezhskii (13) explains how the measurements of Donskoi may be used to obtain a plasma jet conductivity profile. However, the method is quite complex and may be subject to considerable error, as noted above, unless the radius of the jet is known with considerable accuracy. Poberezhskii does not present an example of the method.

Previous immersible probes have disadvantages, too. The radius of the probe of Olson and Lary (4) was large (4mm) compared to the radius of the jet (12.5 mm) in which it was tested. Therefore, the flow perturbation caused by this probe was not negligible. The high heat flux rate caused large coil resistance changes which had to be eliminated by cooling the probe with dry nitrogen. Because of the use of high frequency (13.5 MHz - 23 MHz) power together with the use of electrolytes for calibration, the results of Olson and Lary may be subjet to considerable error. Stubbe (5) has reduced the flow perturbation difficulty of the Olson and Lary design by reducing the diameter of the immersible coil to 1.4 mm, but no provision is made for cooling.

Consequently, the application of this device appears to be limited to a shock tube because high heat flux rates result in undesirable coil resistance changes.

Velocity

As is the case with conductivity, the application of traditional velocity probes to highly energetic ionized gases usually requires considerable modifications and a careful analysis of possible error sources such as ablation effects, shock waves, and relaxation phenomena. Barkan and Whitman (16) have designed and tested a simple expendable plasma pitot tube which yields a Mach number profile of the jet. Other methods use such techniques as photographing the trajectory of injected sparks (17). A theoretical method for computing velocity profiles within the constrictor tube of a constricted-arc wind tunnel has been reported by Stine et al. (18); the method uses experimental tunnel data such as total current, voltage gradient, total heat loss, mass flow, and pressure. Gottschlich et al. (19) have developed a theory whereby knowledge of temperature and thermal conductivity profiles can be used to obtain a velocity profile from the jet centerline out to one-third of the jet radius. Outside this region the relative error becomes large because of possible temperature measurement errors and because asymmetry effects are more pronounced at the boundaries of the jet. Poberezhskii's method of measuring average velocity has already been discussed in the previous section.

A Three-Coil Conductivity/Velocity Probe

Rossow and Posch (20) have developed and tested an immersible, three-coil plasma probe which represents a significant improvement upon previous techniques because it is capable of determining local electrical conductivity and velocity values without greatly perturbing the flow and because it can be used in such a manner that heat-flux sensitivity is negligible. Since the present work is based on the probe design of Rossow and Posch, selected material from Reference 20 will be reviewed in this section.

The basic concepts of the instrument can be understood by referring to Figures 3 and 4 which were prepared by superposition of the

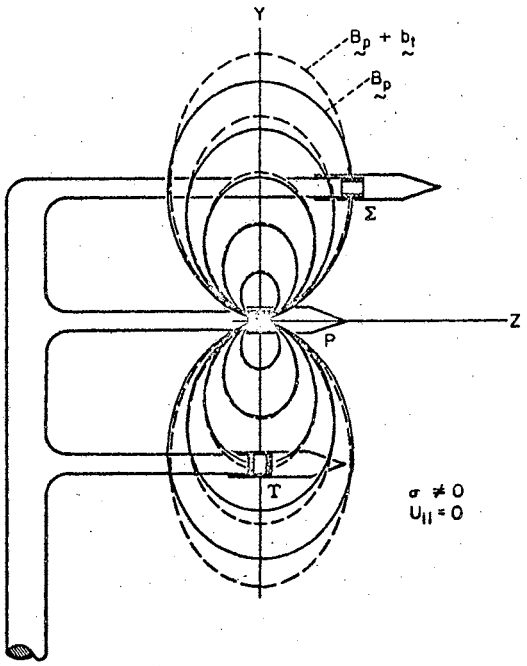

Figure 3. Perturbation of the lines of force for the primary dipole field $\underset{\sim}{B}_p$ caused by the presence of a conducting fluid at rest.

probe onto Figures 2 and 3 of Reference 20. Figure 3 illustrates the principle by which conductivity is measured. Three small coils labeled P for primary, Σ for conductivity, and Y for velocity, lie in the

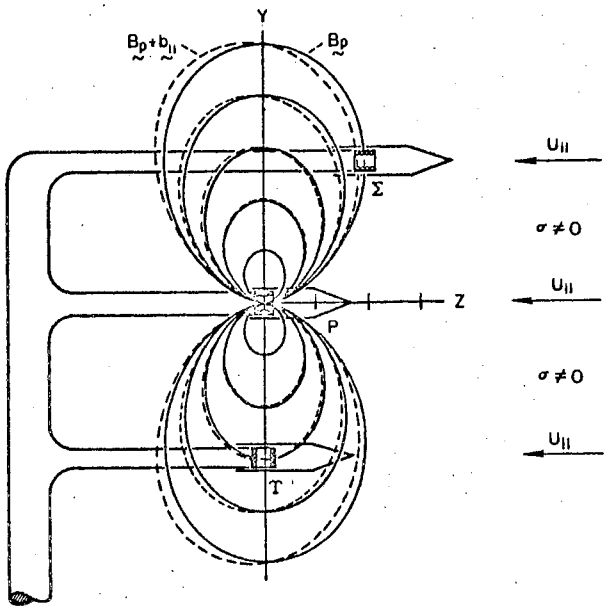

Figure 4. Perturbation of the lines of force for the primary dipole field $\underset{\sim}{B}_p$ caused by the presence and motion of a conducting fluid.

same plane (x = 0) and are mounted on support rods in such a way that the axes of the Σ and P coils are parallel to the z-axis while the axis of the Y coil is parallel to the y-axis.

In the absence of a conducting or a dielectric medium, the pulsating current in the primary coil produces a magnetic field which may be approximated by an oscillating ideal magnetic dipole field. The solid

lines labeled $\underset{\sim}{B}_p$ indicate the shape of the lines of force for the primary dipole field at an instant in time. Under these circumstances it can be seen that the primary field produces no flux linkage at either the Σ coil or the Y coil. However, in the presence of a conducting, quiescent medium, the primary magnetic field induces currents which, in turn, create a perturbation magnetic field designated as $\underset{\sim}{b}_t$. The dotted lines indicate an instantaneous position of the lines of force for the resultant magnetic field (primary plus perturbation) which does produce flux linkage at the Σ coil while the coil is still free of flux linkage due to its orientation.

Similarly, in Figure 4, the dotted lines indicate a particular instantaneous position of the lines of force for the resultant magnetic field which is the sum of the primary field $\underset{\sim}{B}_p$ and a perturbation field $\underset{\sim}{b}_{||}$ caused by the motion of a conducting fluid across the primary lines of force. As the sketch shows, the resultant field produces flux linkage at the Y coil while the Σ coil flux linkage is zero for such a disturbance.

Since the perturbation fluxes at the two secondary coils are time dependent, Faraday's law of induction implies that the potential output of the Σ coil will be proportional to the magnitude of the z-component of the field perturbation caused by the conductivity σ and the potential output of the Y coil will be proportional to the magnitude of the y-component of the field perturbation caused by the product of the conductivity σ and velocity $U_{||}$ or $\sigma U_{||}$.

The theoretical analysis of Rossow and Posch begins with Maxwell;s equations

$$\underset{\sim}{\nabla} \cdot \underset{\sim}{B} = 0, \qquad \underset{\sim}{\nabla} \cdot \underset{\sim}{E} = 0, \tag{5}$$

$$\underset{\sim}{\nabla} \times \underset{\sim}{B} = \mu \underset{\sim}{J}, \tag{6}$$

$$\underset{\sim}{\nabla} \times \underset{\sim}{E} = - \frac{\partial \underset{\sim}{B}}{\partial t}, \tag{7}$$

the simplified Ohm's law

$$\underset{\sim}{J} = \sigma(\underset{\sim}{E} + \underset{\sim}{U} \times \underset{\sim}{B}), \tag{8}$$

the conservation of charge equation for a neutral plasma

$$\underset{\sim}{\nabla} \cdot \underset{\sim}{J} = 0, \tag{9}$$

and the Coulomb or transverse-gage condition

$$\underset{\sim}{\nabla} \cdot \underset{\sim}{A} = 0. \tag{10}$$

In these equations $\underset{\sim}{E}$ is the electric field intensity vector, $\underset{\sim}{B}$ is the magnetic induction vector, $\underset{\sim}{J}$ is the current density vector, $\underset{\sim}{U}$ is the plasma velocity vector, σ is the electrical conductivity, μ is the permeability, and $\underset{\sim}{A}$ is a vector potential function such that

$$\underset{\sim}{B} = \underset{\sim}{\nabla} \times \underset{\sim}{A}. \tag{11}$$

To obtain a solution for these equations, Rossow and Posch have imposed the following restrictions

1. The flow field is unbounded.
2. The electrical conductivity and velocity are taken to be constant over the entire flow field.

3. The only applied field is $\underset{\sim}{B}_p$ which is that magnetic field created by the oscillating current in the primary coil.

4. Since the magnitude of $\underset{\sim}{B}_p$ is less than 10^{-8} gauss, the representation of conductivity as a scalar quantity is justifiable. (In the presence of large applied fields, the conductivity of a plasma assumes a tensorial form.)

5. The small magnitude of $\underset{\sim}{B}_p$ also justifies the representation of the resultant magnetic field, $\underset{\sim}{B}$, as a power series expansion in the magnetic Reynolds number, R_m. As mentioned in Chapter I, typical values of R_m for constricted-arc wind tunnels range from 10^{-4} to 10^{-1} so that neglect of terms of order R_m^2 is reasonable.

6. Radiation effects are neglected.

7. In Equation (6) the displacement current term is neglected. Omission of this term is justified below in Appendix C.

As a zeroth-order approximation for $\underset{\sim}{B}$, Rossow and Posch used the primary dipole field $\underset{\sim}{B}_p$ which would be produced by an idealized primary coil in free space. The vector potential $\underset{\sim}{A}_p$ for such a field is well known and appears on page 237 of Stratton (22) as

$$\underset{\sim}{A}_p(x,y,z,t) = \frac{\mu}{4\pi} \underset{\sim}{m} \times \underset{\sim}{\nabla}\left(\frac{1}{r}\right) \tag{12}$$

where $\underset{\sim}{m}$ is the magnetic dipole moment of the idealized primary coil located at $(x,y,z) = (0,0,0)$, and $r = (x^2 + y^2 + z^2)^{\frac{1}{2}}$. Thus, Equation (11) yields the solution

$$\underset{\sim}{B}_p = \underset{\sim}{\nabla} \times \underset{\sim}{A}_p \ . \tag{13}$$

Since $\underset{\sim}{B}_p$ is time dependent, Equation (7) requires the existence of an associated electric field, denoted by subscript t, such that

$$\underset{\sim}{\nabla} \times \underset{\sim}{E}_t = - \frac{\partial \underset{\sim}{B}_p}{\partial t} \tag{14}$$

and this equation may be solved for $\underset{\sim}{E}_t$.

Equation (8) suggests that the total current may be considered as the sum of two components, the first of which is

$$\underset{\sim}{J}_t = \sigma \underset{\sim}{E}_t \ , \tag{15}$$

and the second is

$$\underset{\sim}{J}_{||} = \sigma \underset{\sim}{U} \times \underset{\sim}{B}_p = \sigma U_{||} \underset{\sim}{k} \times \underset{\sim}{B}_p \tag{16}$$

where $\underset{\sim}{U} = U_{||} \underset{\sim}{k}$ as in Figure 4 and the unit vectors $\underset{\sim}{i}$, $\underset{\sim}{j}$, $\underset{\sim}{k}$ are directed in the positive x,y,z directions, respectively. The first component, $\underset{\sim}{J}_t$, is caused by the application of an electric field, $\underset{\sim}{E}_t$, to a stationary conducting fluid. The second component, $\underset{\sim}{J}_{||}$, arises from the motion $U_{||} \underset{\sim}{k}$ of a conducting fluid across lines of force, $\underset{\sim}{B}_p$.

The analysis of Reference 20 continues by using Equation (6) to solve for the first-order perturbation fields $\underset{\sim}{b}_t$ and $\underset{\sim}{b}_{||}$ which accompany $\underset{\sim}{J}_t$ and $\underset{\sim}{J}_{||}$. Thus, the resultant magnetic field, including first-order terms only, is

$$\underset{\sim}{B} = \underset{\sim}{B}_p + \underset{\sim}{b}_t + \underset{\sim}{b}_{||} \ . \tag{17}$$

This equation, together with Equations (6), (7), and (8), could be used to solve for currents and perturbation fields of higher order in R_m. However, as previously mentioned, the terms of higher order may be neglected in the present case because R_m is small.

For future reference, the following solutions are listed from Reference 20:

$$\underset{\sim}{B}_p = -m \cos \omega t \left[\underset{\sim}{i} \frac{3xz}{r^5} + \underset{\sim}{j} \frac{3yz}{r^5} + \frac{\underset{\sim}{k}}{r^3} \left(\frac{3z^2}{r^2} - 1 \right) \right] \tag{18}$$

$$\underset{\sim}{E}_t = -\omega m \sin \omega t \underset{\sim}{\nabla} \times \left(\frac{\underset{\sim}{k}}{r} \right) \tag{19}$$

$$\underset{\sim}{J}_t = -\sigma \omega m \sin \omega t \left[\underset{\sim}{i} \left(\frac{-y}{r^3} \right) + \underset{\sim}{j} \left(\frac{x}{r^3} \right) \right] \tag{20}$$

$$\underset{\sim}{J}_{||} = 3U_{||} m \cos \omega t \left[\underset{\sim}{i} \frac{yz}{r^5} - \underset{\sim}{j} \frac{xz}{r^5} \right] \tag{21}$$

$$\underset{\sim}{b}_t = -\frac{\sigma \mu \omega m}{2} \sin \omega t \left[\underset{\sim}{i} \frac{xz}{r^3} + \underset{\sim}{j} \frac{yz}{r^3} + \underset{\sim}{k} \frac{r^2 + z^2}{r^3} \right] \tag{22}$$

$$\underset{\sim}{b}_{||} = \frac{\sigma \mu U_{||} m}{2} \cos \omega t \left[1 - \frac{3z^2}{r^2} \right] \left[\underset{\sim}{i} \frac{x}{r^3} + \underset{\sim}{j} \frac{y}{r^3} + k \frac{z}{r^3} \right] \tag{23}$$

$$m = (n_p r_p^2) \mu I_p / 4 \tag{24}$$

where I_p is the peak current supplied at frequency ω to the n_p-turn primary coil whose characteristic radius is r_p.

Equations (18) through (24), plus Faraday's law of induction, dictate the locations of the secondary coils Σ and Y. Faraday's law states that the potential Φ_s induced on a secondary anywhere in the flow field may be approximated by

$$\Phi_s = -\pi n_s r_s^2 \frac{\partial}{\partial t} \left(\underset{\sim}{B} \cdot \underset{\sim}{N}_s \right) \tag{25}$$

where r_s is the characteristic radius of the n_s-turn secondary, $\underset{\sim}{B}$ is the resultant field evaluated at the center of the coil, and $\underset{\sim}{N}_s$ is a unit vector parallel to the axis of the coil. Thus, if the center of

the Σ coil is located at $(x,y,z) = (0,y_\Sigma,y_\Sigma/\sqrt{2})$ and is oriented such that $\underset{\sim}{N}_\Sigma = \underset{\sim}{k}$, then Equations (22) and (25) may be combined to obtain

$$\Phi_{\Sigma\infty} = (n_\Sigma r_\Sigma^2)(n_p r_p^2)(\mu\omega)^2 \frac{\pi I_p \sigma}{6\sqrt{3/2}\, y_\Sigma} \cos \omega t \qquad (26)$$

where ∞ refers to an unbounded medium. Similarly, if the center of the Y coil is located at $(x,y,z) = (0,-y_\Sigma,0)$ such that $\underset{\sim}{N}_Y = \underset{\sim}{j}$, then the potential induced on the Y coil in an unbounded medium will be

$$\Phi_{Y\infty} = -(n_Y r_Y^2)(n_p r_p^2) \frac{\mu^2 \omega \pi I_p \sigma U_{11}}{8 y_\Sigma^2} \sin \omega t \ . \qquad (27)$$

Equation (27) represents the potential that would be induced on the Σ secondary if the probe of Figure 3 were immersed in an infinite conducting medium. However, currents cannot flow through the regions occupied by the probe itself. Equation (20) indicates that the strength of the induced currents decreases as r^{-2} so that only the region occupied by the primary coil support rod and coil shield contributes to a significant loss of signal at the secondary coil. This loss had been calculated by Rossow and Posch for both secondaries and the corrections are reproduced in Figure 5. The abscissa is $2\rho_o/y_\Sigma$ where ρ_o is the support rod radius and y_Σ is the coil spacing defined above. The ordinates K_Σ and K_Y represent factors by which the oscilloscope readings Φ_Σ and Φ_Y must be multiplied to account for the loss of signal.

Figure 6 is a sketch of the electrical circuit which was used for the probes tested by Rossow and Posch. The primary coil is supplied with power (0.1 amp, 15 volts) from a 100-kHz crystal-controlled oscillator by means of shielded litz wires. The signal induced on the Σ

coil is first amplified by a factor of 5 in a solid-state differential amplifier, then conditioned by a magnetostrictive filter with a ±15 Hz

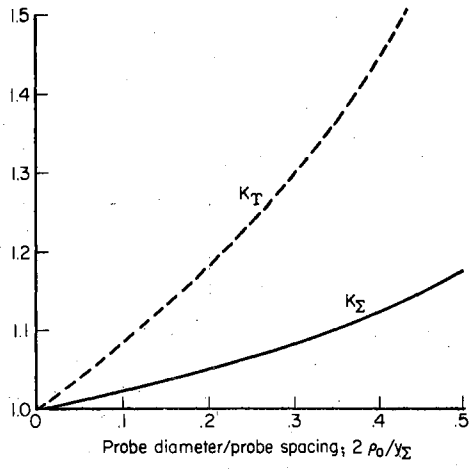

Figure 5. Factors used to correct secondary voltages for loss of signal caused by the presence of the primary-coil support rod. (Reference 20)

bandpass to reduce amplifier and plasma stream noise, and, finally, displayed on a dual-beam cathode ray oscilloscope. The signal from the Y coil receives identical treatment. Like the primary circuit, the secondary circuits make use of shielded litz wires. The shields of all three circuits are connected to a common ground.

As shown in Figure 6, each of the tickler coils is a transformer consisting of one turn of secondary circuit wire, two turns of primary

circuit wire, and a brass or a ferrite core. The directions of the windings are also indicated in the figure. The function of the tickler

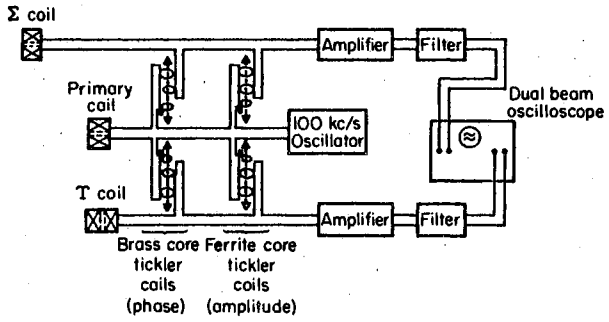

Figure 6. Electrical circuit used in tests of probes by Rossow and Posch. (Reference 20)

coils is to induce in the secondary circuits signals which null out unwanted signals picked up by the coils when the probe is held in room air. The spurious signals may be caused by slight misalinement of the coils, stray noise and capacitance, or by the fact that the actual field of the primary coil of finite size deviates slightly from the field produced by the ideal magnetic dipole upon which the theory is based. The axial position of the brass core determines the phase of the null signal while the axial position of the ferrite core determines the amplitude of the null signal.

The probe may be calibrated by one of two methods. The first method is based on the theoretical analysis and involves displacements of the coils in the z-direction relative to the primary coil. If, for

example, the Σ coil is moved from its design location at $(x,y,z) = (0,y_\Sigma,y_\Sigma/\sqrt{2})$ to a calibration position at $(x,y,z) = (0,y_\Sigma,0)$ with no change in orientation, then the output of the Σ coil in free space may be computed from Equations (18) and (25) and the peak-to-peak signal at the oscilloscope will be

$$\Phi_{\Sigma cal} = K_e\left[I_p(n_p r_p^2)(n_\Sigma r_\Sigma^2)\right]\frac{2\pi\mu\omega}{4y_\Sigma^3} \equiv K_e K_g \frac{2\pi\mu\omega}{4y_\Sigma^3} \tag{28}$$

where K_e represents the total amplification factor for the electrical circuit and the coil parameter factor K_g is defined as

$$K_g = I_p(n_p r_p^2)(n_\Sigma r_\Sigma^2)$$

so that

$$K_e K_g = \Phi_{\Sigma cal}\frac{4y_\Sigma^3}{2\pi\mu\omega}\,. \tag{29}$$

Now, if the probe with its coils located in the design positions were immersed in an infinite medium of constant conductivity, then the signal Φ_Σ displayed at the oscilloscope would be

$$\Phi_\Sigma = K_e K_\Sigma \Phi_{\Sigma\infty} \tag{30}$$

and, by introducing Equations (28) and (29) and rearranging, Equation (30) becomes

$$\sigma = \Phi_\Sigma\left[\frac{3\sqrt{6}\,K_\Sigma}{4\mu\omega y_\Sigma^2 \Phi_{\Sigma cal}}\right] \tag{31}$$

where the numerical value of the factor in brackets is called the conductivity calibration constant. It should be emphasized that Equation (31) is restricted to an unbounded medium of constant conductivity.

In a similar manner the method may be extended to the Y coil by recording its free-space output Φ_{Ycal} when the Y coil has been moved from $(x,y,z) = (0,-y_\Sigma,0)$ to $(x,y,z) = (0,-y_\Sigma,-y_\Sigma/2)$. Proceeding as above and utilizing Equation (31), the following equations may be derived:

$$\sigma U_{||} = \Phi_Y\left[\frac{96\sqrt{5}\ K_Y}{125\mu y_\Sigma \Phi_{Ycal}}\right] \tag{32}$$

$$U_{||} = \frac{\Phi_Y}{\Phi_\Sigma}\left[\frac{\Phi_{\Sigma cal}}{\Phi_{Ycal}}\frac{K_Y}{K_\Sigma}\frac{128\omega y_\Sigma}{25\sqrt{30}}\right] \tag{33}$$

The second calibration method is based on experiment. The preceding discussion implies that the oscilloscope signal Φ_Σ for an unbounded medium of constant conductivity σ is a function of four parameters such that

$$K_\Sigma \Phi_\Sigma = K_e K_c \sigma \tag{34}$$

where K_e and K_Σ are defined above and K_c is a coil parameter factor which includes such quantities as $n_p r_p^2$, $n_\Sigma r_\Sigma^2$, I_p, μ, and ω; note that K_c of Equation (34) is similar but not equal to the K_g defined in Equation (28). Equation (34) may be modified to account for the existence of a cylindrical boundary by introducing a correction factor Θ_Σ which, if the probe is at the center of the cylinder, is a function of coil spacing y_Σ divided by the cylinder radius R. Therefore, Equation (34) becomes

$$K_\Sigma \Phi_\Sigma = K_e K_c \Theta_\Sigma (y_\Sigma/R)\sigma \tag{35}$$

and as R increases without bound, Θ_Σ must approach unity. Thus, if

the probe is immersed in the center of several deep cylindrical containers of varying radii filled with an electrolyte of known σ, then the corresponding scope readings, corrected for loss of signal, may be plotted vs. R^{-1}. If the containers are large enough, the plotted points are linear and may be extrapolated to $R^{-1} = 0$. If $[K_\Sigma \Phi_\Sigma]_{R^{-1}=0}$ represent the extrapolated intercept, then Equation (35) yields

$$K_e K_c = \frac{\left[K_\Sigma \Phi_\Sigma\right]_{R^{-1}=0}}{\sigma} \tag{36}$$

because $\Phi_\Sigma(0) = 1$. Therefore, Equation (34) may be rearranged to read

$$\sigma = \Phi_\Sigma\left[\frac{K_\Sigma}{K_e K_c}\right] \tag{37}$$

and the factor in brackets, the conductivity calibration constant, is determined by Equation (36) and Figure 5.

Rossow and Posch constructed and calibrated three probes. Table I is a summary of the theoretical and experimental values for the calibration constants for the three probes.

TABLE I

CHARACTERISTICS OF PROBES TESTED

Probe Number	Coil Spacing, y_Σ, mm	Coil and Rod Diameter, $2\rho_o$, mm	σ/Φ_Σ, mho/mV-m		$U_{\|\|}\Phi_\Sigma/\Phi_Y$, m/sec
			Experimental	Theoretical	Theoretical
I	22	6.4	209	221	6,100
II	22	2.0	3000	---	14,600
III	8	2.0	613	610	3,300

The theoretical constant for Probe II was not determined. The agreement between the experimental and theoretical conductivity constants serves to confirm the theoretical analysis of Rossow and Posch. As shown in Chapter IV, Equations (31) and (32) may be applied to probe data taken along a diameter of a cylindrical jet to obtain conservative estimates for the actual σ and $\sigma U_{||}$ profiles.

All three probes were tested by Rossow and Posch in an argon plasma jet generated by a 1.27-cm constricted-arc wind tunnel; the findings of those tests are briefly reviewed in the following paragraphs. Figure 7(a) shows Probe I mounted on the air-driven dolly which swept the device along a horizontal diameter of the free supersonic jet. The circular exit plane of the converging-diverging nozzle is shown to the right of the probe. The vertical main support cylinder was made of brass and was covered with Teflon. Initially, the horizontal coil support rods were made of Teflon and this construction proved to be unsatisfactory because the high heat flux caused the rods to droop. This difficulty was overcome by using ceramic support rods. Figure 7(b) shows Probes I and II equipped with ceramic rods and Teflon heat shields. Silicone rubber was also tried as a heat shield material but was not as suitable as Teflon because the silicone rubber shields had a tendency to form a conducting char layer that probably caused inconsistent data and short-circuiting of several coils. To assure fore-and-aft symmetry of the induced currents $\underset{\sim}{J}_t$ and $\underset{\sim}{J}_{||}$, it was found that the heat shields should extend from two to four coil diameters ahead of the coils in the upstream direction.

The arc current, I_{arc}, was varied from 100 to 400 amps and the other tunnel variables were such that the jet was supersonic throughout

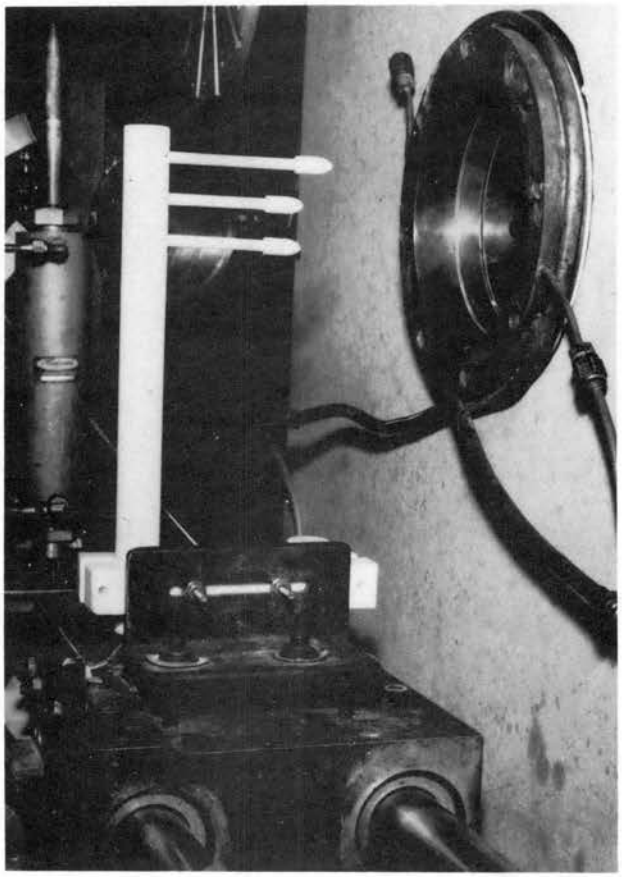

Figure 7(a). Probe I mounted on a traversing carriage near the nozzle exit. (Courtesy of Rossow and Posch)

this range. Conductivity data were obtained with Probe I over the range $100 \leq I_{arc} \leq 400$ amp and with Probes II and III over the range

$150 \leq I_{arc} \leq 400$ amp. It was estimated that the lowest measurable value of conductivity for Probe I was 1.0 mho/meter and 10 mho/meter for Probes II and III.

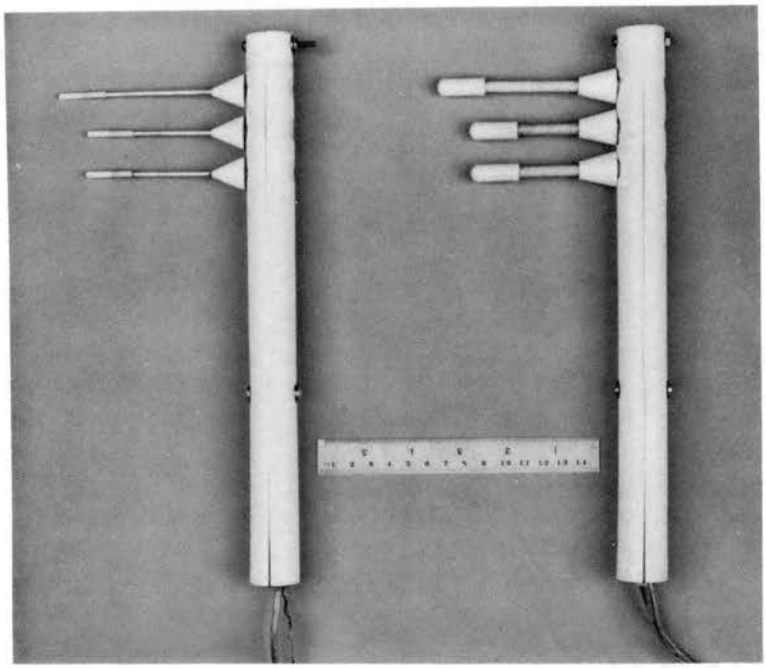

Figure 7(b). Probe II is on the left and Probe I is on the right. (Courtesy of Rossow and Posch)

All three probes yielded well-defined conductivity recordings. When Rossow and Posch applied Equation (37) to centerline values of Φ_Σ taken by the three probes under the same tunnel operating conditions, the computed values of σ agreed within about 10 percent. The velocity recordings obtained with Probes I and II were also well defined. A

few reasonable velocity records were obtained with Probe III before the Y coil developed a short circuit.

Probe II was tested with a series of Teflon cone-cylinder heat shields, each having different cone half-angles, in an effort to ascertain the effects of shock-wave and boundary-layer interactions on the recorded data. The outside diameter of each shield was 3.16 mm and the inside diameter was 2.0 mm. Half-angles tested were 5°, 10°, 20°, 30°, and 40° and each shield extended at least 4.0 mm beyond the coil in the upstream z direction to assure the necessary fore and aft symmetry. The probe was swept through the stream in less than 0.3 second because it had been experimentally determined that the Teflon cones would begin to ablate appreciably if exposed to the jet for more than 0.5 second. Ablation should be avoided because the ablation products may cause a large change in the electrical conductivity of the adjacent boundary layer. The data obtained with the different cone-cylinder heat shields did not differ in any important details. This result indicated that neither the conductivity nor the velocity data of Probe II was significantly affected by the shock-wave sweepback or boundary-layer interaction over the range of flows tested.

Additional coil design information for Probe II is as follows:

	P	Y	Σ
Minimum Diameter, mm	2.0	2.0	2.0
Maximum Diameter, mm	4.0	4.0	4.0
Number of Turns	122	175	700
Wire Size (Copper, Enameled), mm	#38 AWG	.038	.038

The coil forms on which the wires are wound should be nonconducting and should have a low coefficient of thermal expansion. Shielded litz should be used to connect the coils to the external circuitry. To prevent the possible existence of electrostatic coupling with the primary coil or plasma stream, the secondary coils and all metal components should be independently shielded and, to prevent electrical leakage, all hollow spaces should be filled with a suitable potting material such as silicone rubber. It was found that the shields should not be allowed to contact each other except at some convenient ground in the external circuitry.

Concerning heat flux sensitivity, the oscilloscope tracings obtained by Rossow and Posch did exhibit some asymmetry with respect to the centerline of the jet (see Figure 16). However, this asymmetry was caused by the response time of the probe system. A two-way sweep of the instrument produced, by superposition of recordings, a symmetric signal tracing.

By way of summary, the probe design of Rossow and Posch offers the following advantages:

1. The instrument can be used to obtain local values of conductivity and velocity by a method to be outlined in Chapter IV.
2. The design of Probe II has virtually eliminated the heat flux sensitivity and flow perturbation problems of previous immersible instruments.
3. Although the impressed frequency is comparatively low, the sensitivity of the probe is as great as or greater than that of previous immersible instruments. The use of low-frequency

impressed power decreases the complications caused by stray capacitance and allows omission of the displacement current term.

4. Because of the simplicity of the probe and its components, the fabrication, construction, and assembly of the instrument system are within the capability of any research laboratory having a modest machine shop and an oscilloscope.

CHAPTER III

FIELD EQUATIONS FOR A CYLINDRICAL CONDUCTING FLUID

As mentioned in Chapter II, the theory of Rossow and Posch (20) decoupled the perturbation magnetic fields by neglecting terms of order R_m^2, assumed σ and $U_{||}$ to be constant and uniform, and considered only an unbounded medium. This chapter presents modifications of the previous theory by recognizing the presence of a cylindrical boundary of radius R such that the plasma occupies the region

$$x^2 + y^2 \leq R^2 \; ; \qquad -\infty < z < \infty \; .$$

Also, the position of the probe will not be restricted to the center of the cylindrical region. Furthermore, for this part of the analysis it is assumed that σ and $U_{||}$ are constant and uniform in the region occupied by the plasma and that these quantities vanish elsewhere. The present analysis will also ignore terms of order R_m^2, the displacement current, and relativistic effects. The only applied field is $\underset{\sim}{B}_p$, which is caused by the oscillating current in the primary coil and this field, being of the order 10^{-8} gauss, is so small that the assumption of scalar conductivity is well justified.

Electrical Conductivity

The analysis begins with a consideration of the basic equations which are identical, except for the boundary conditions, to those of Chapter II (see Equations (5) through (11)).

Because σ and $U_{||}$ vanish outside the cylinder, the two boundary conditions on the current density vector are

$$\underset{\sim}{J} = \underset{\sim}{0} \quad \text{whenever} \quad x^2 + y^2 > R^2 \tag{38}$$

$$\underset{\sim}{J} \cdot \underset{\sim}{N}_{\perp} = 0 \quad \text{for} \quad x^2 + y^2 = R^2 \tag{39}$$

where $\underset{\sim}{N}_{\perp}$ is a unit vector which is perpendicular to the cylindrical boundary.

If Equation (11) is substituted into Equation (6), the result will be

$$\underset{\sim}{\nabla} \times \underset{\sim}{\nabla} \times \underset{\sim}{A} = \mu \underset{\sim}{J} \tag{40}$$

and if this expression is expanded so that Equation (10) may be applied, then the final result will be

$$\nabla^2 \underset{\sim}{A} = -\mu \underset{\sim}{J} \tag{41}$$

where it is understood that the Laplacian operates on each rectangular component of $\underset{\sim}{A}$. Equation (41) represents a condensation of the three Maxwell equations. Therefore, the problem reduces to the solution of Equations (8) and (41) subject to the boundary conditions of Equations (38) and (39).

The solution to Equation (41) is unique and it may be solved by finding a Green's function or by an equivalent technique, the method of images (see, for example, Chapter 2 of Reference 23). The latter method was chosen because it appears to be a simpler approach and it makes use of Equations (18) through (24) from Chapter II.

It is also convenient to use an analogy based on the steady, two-dimensional flow of an incompressible fluid for which there exists a potential function Ψ, called the stream function, such that the velocity field $\underset{\sim}{U}$ is given by

$$\underset{\sim}{U} = \underset{\sim}{\nabla} \times \underset{\sim}{k}\Psi \tag{42}$$

An important property of the stream function is the fact that lines of constant Ψ are streamlines.

This analogy may be used to represent the two-dimensional current density vector field as

$$\underset{\sim}{J} = \underset{\sim}{\nabla} \times \underset{\sim}{k}\psi \tag{43}$$

so that current paths or loops will coincide with lines of constant ψ.

Returning to the method of images, consider the geometry of Figure 8 where the medium is assumed to be unbounded, at rest, and of uniform and constant σ. If the real coil is located at $(x,y,z) = (a,0,0)$, then an image system of strength $\mathbf{A}$ located at $(x,y,z) = (-a,0,0)$, must be found such that one of the induced current loops will coincide with the dashed cylinder and thereby satisfy one of the boundary conditions.

The current, $\underset{\sim}{J}_{tr}$, induced by the real coil is given by Equation (20) which, for the present case, becomes

$$\underset{\sim}{J}_{tr} = -G_t\left[\underset{\sim}{i}\left(\frac{-y}{r^3}\right) + \underset{\sim}{j}\left(\frac{x - a}{r^3}\right)\right] \tag{44}$$

where

$$G_t = \sigma\omega m \sin \omega t$$

and

$$r^2 = (x - a)^2 + y^2 + z^2 .$$

Therefore, a real stream function for $\underset{\sim}{J}_{tr}$ is

$$\psi_{tr} = -G_t[(x - a)^2 + y^2 + z^2]^{-1/2} \tag{45}$$

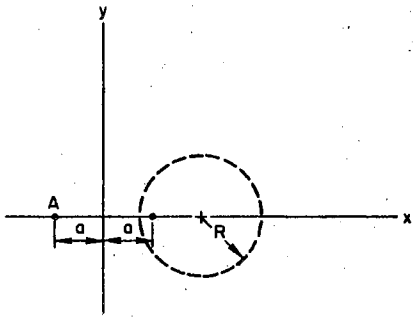

Figure 8. Relation between real and image dipole locations.

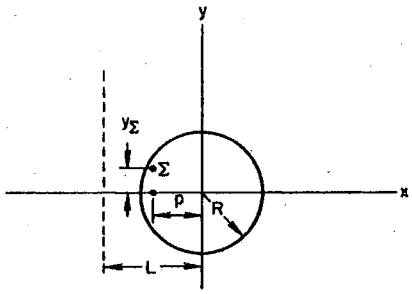

Figure 9. Probe location inside the cylindrical boundary.

By trial and error, a stream function

$$\psi_{ti} = \mathbb{A} G_t[(x + a)^2 + y^2 + \mathbb{A}^2 z^2]^{-1/2} \tag{46}$$

was found for the image system so that the resultant stream function is

$$\psi_t = -G_t\{[(x - a)^2 + y^2 + z^2]^{-1/2} - \mathbb{A}[(x + a)^2 + y^2 + \mathbb{A}^2 z^2]^{-1/2}\} \tag{47}$$

and the total induced current becomes $\underset{\sim}{J}_t = \underset{\sim}{\nabla} \times \underset{\sim}{k}\psi_t$. This expression for ψ_t is particularly useful because the surface defined by the condition $\psi_t \equiv 0$ happens to be the cylindrical surface

$$\left[x - a\left(\frac{\mathbb{A}^2 + 1}{\mathbb{A}^2 - 1}\right)\right]^2 + y^2 = \left(\frac{2a\mathbb{A}}{\mathbb{A}^2 - 1}\right)^2 \tag{48}$$

so that the current loops corresponding to $\psi_t = 0$ meet the requirement specified by Equation (39).

Referring to Figure 9, it is desirable to translate the y-axis to the center of the jet of radius R. Figure 9 illustrates the locations of the real primary and secondary Σ coils after the y-axis has been translated a distance $L = a(\mathbb{A}^2 + 1)/(\mathbb{A}^2 - 1)$, that is, to the center of the jet. Since $L - a = p$ and $R = 2a\mathbb{A}/(\mathbb{A}^2 - 1)$, a and $\mathbb{A}$ may be solved as functions of R and p with the result that

$$a = (R^2 - p^2)/2p \tag{49}$$

$$\mathbb{A} = R/p \ . \tag{50}$$

If these expressions are substituted into Equation (47) and if the y-axis is translated a distance L, then it follows that

$$\psi_t = -G_t[(\overline{x + p}^2 + y^2 + z^2)^{-1/2} - R(\overline{px + R^2}^2 + p^2y^2 + R^2z^2)^{-1/2}] \ . \tag{51}$$

Therefore, the final expression for the resultant current density vector is

$$\underset{\sim}{J}_t = \underset{\sim}{\nabla} \times \underset{\sim}{k}\Psi_t$$

$$= -G_t\left\{\underset{\sim}{i}\left[\frac{R^2p^2y}{(\overline{px+R^2}^2 + p^2y^2 + R^2z^2)^{3/2}} - \frac{y}{(\overline{x+p}^2 + y^2 + z^2)^{3/2}}\right]\right.$$

$$\left. - \underset{\sim}{j}\left[\frac{Rp(px + R^2)}{(\overline{px+R^2}^2 + p^2y^2 + R^2z^2)^{3/2}} - \frac{x + p}{(\overline{x+p}^2 + y^2 + z^2)^{3/2}}\right]\right\} . \quad (52)$$

Equation (6) may now be used to obtain $\underset{\sim}{b}_t$ from the relation

$$\underset{\sim}{\nabla} \times \underset{\sim}{b}_t = \mu \underset{\sim}{J}_t , \quad (53)$$

by use of Equation (11), page 231 of Reference 22. That is, the perturbation field, $\underset{\sim}{b}_t$, at any field point (x',y',z') in the cylindrical plasma is given as

$$\underset{\sim}{b}_t(x',y',z',t) = \frac{\mu}{4\pi} \int_{-\infty}^{\infty} \int_{-R}^{R} \int_{-\sqrt{R^2-y^2}}^{\sqrt{R^2-y^2}} \underset{\sim}{J}_t(x,y,z,t) \times \underset{\sim}{\nabla} r^{-1} \, dx \, dy \, dz \quad (54)$$

where $r = (\overline{x - x'}^2 + \overline{y - y'}^2 + \overline{z - z'}^2)^{1/2}$. Note that the current density vector $\underset{\sim}{J}_t$ does not vanish outside of the cylindrical region as required by Equation (38). However, this requirement is satisfied by Equation (54) because the limits of integration do not extend beyond the cylindrical boundary so that the mathematical current loops outside of the cylinder cannot contribute to $\underset{\sim}{b}_t$. Since the axis of the Σ coil is parallel to $\underset{\sim}{k}$, only the z component of $\underset{\sim}{b}_t$ will be used in Faraday's law, Equation (25). Noting that $(x',y',z') = (-p, y_\Sigma, y_\Sigma/\sqrt{2})$, the z component of $\underset{\sim}{b}_t$ must be

$$b_{zt} = \frac{\mu G_t}{4\pi}\int_{-\infty}^{\infty}\int_{-R}^{R}\int_{\sqrt{R^2-y^2}}^{\sqrt{R^2-y^2}}\left\{R_p\left[\frac{py(y-y_\Sigma)+(px+R^2)(x+p)}{\left(\overline{x+p}^2+\overline{y-y_\Sigma}^2+z-\frac{\overline{y_\Sigma}^2}{\sqrt{2}}\right)^{3/2}\left(\overline{px+R^2}^2+p^2y^2+R^2z^2\right)^{3/2}}\right]\right.$$

$$\left.-\left[\frac{y(y-y_\Sigma)+(x+p)^2}{\left(\overline{x+p}^2+\overline{y-y_\Sigma}^2+z-\frac{\overline{y_\Sigma}^2}{\sqrt{2}}\right)^{3/2}\left(\overline{x+p}^2+y^2+z^2\right)^{3/2}}\right]\right\}dx\,dy\,dz \qquad (55)$$

If the variables x, y, z and parameters p, y in the last equation are nondimensionalized with respect to the jet radius R, then it follows that

$$b_{zt} = \frac{\mu G_t}{R}\int_{-\infty}^{\infty}\int_{-1}^{1}\int_{-\sqrt{1-Y^2}}^{\sqrt{1-Y^2}}\left\{\left[\frac{P^2Y(Y-S)+P(X+P)(PX+1)}{\left(\overline{X+P}^2+\overline{Y-S}^2+\overline{Z-D}^2\right)^{3/2}\left(\overline{PX+1}^2+P^2Y^2+Z^2\right)^{3/2}}\right]\right.$$

$$\left.-\left[\frac{Y(Y-S)+(X+P)^2}{\left(\overline{X+P}^2+\overline{Y-S}^2+\overline{Z-D}^2\right)^{3/2}\left(\overline{X+P}^2+Y^2+Z^2\right)^{3/2}}\right]\right\}dX\,dY\,dZ \qquad (56)$$

where $X = x/R$, $Y = y/R$, $Z = z/R$, $P = p/R$, and $S = y_\Sigma/R$. Substitution of this expression into Faraday's law yields

$$\Phi_\Sigma = -(n_\Sigma r_\Sigma^2)(n_p r_p^2)(\mu\omega)^2\,\frac{I_p\sigma\cos\omega t}{16R}\int_{-\infty}^{\infty}\int_{-1}^{1}\int_{-\sqrt{1-Y^2}}^{\sqrt{1-Y^2}}F_\Sigma\,dX\,dY\,dZ \qquad (57)$$

where F_Σ is used to denote the complicated integrand of the preceding expression. In order to eliminate the probe and coil characteristics, Equation (57) is made dimensionless by dividing it by Equation (26) to obtain

$$\frac{\Phi_\Sigma}{\Phi_{\Sigma\infty}} \equiv \Theta_\Sigma(S,P) = -\frac{3\sqrt{6}}{16\pi}\,S\int_{-\infty}^{\infty}\int_{-1}^{1}\int_{-\sqrt{1-Y^2}}^{\sqrt{1-Y^2}}F_\Sigma\,dX\,dY\,dZ\,. \qquad (58)$$

Note that if $P = 0$, then Θ_Σ as defined by Equation (58) is the same

as the function $\Theta_\Sigma(y_\Sigma/R)$ of Equation (35). For a given probe, the conductivity correction factor Θ_Σ represents the ratio of the signal which would be induced in a finite cylindrical region having a constant conductivity to the signal which would be induced in an infinite region having the same constant conductivity.

As might be anticipated, the integrals of Equation (58) cannot be evaluated readily in closed form. Although one integration could be accomplished, it was more convenient to evaluate the integrals numerically rather than deal with the elliptic integrals which would result from the analytical integration. Therefore, Equation (58) was evaluated using a numerical 10-point Gaussian-quadrature computer program which is described in Appendix B. The results of the computation are presented in Figures 10 and 11. Figure 10 is a plot of Θ_Σ vs. $P = p/R$ for four

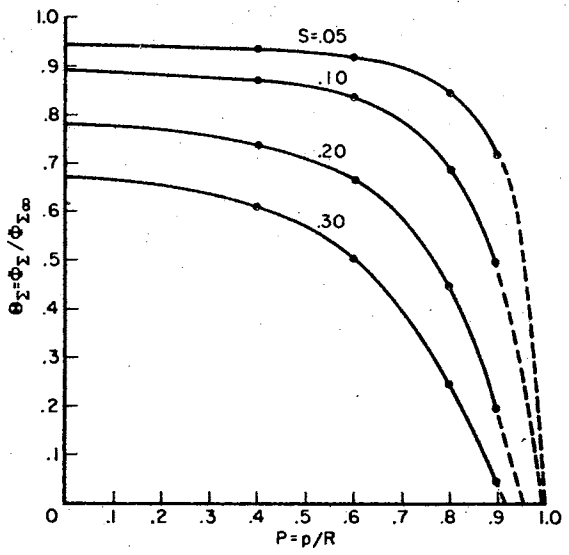

Figure 10. Conductivity correction factor as a function of radial position of the probe for several values of the coil spacing parameter S.

values of the parameter $S = y_\Sigma/R$; the dashed portions of the curves represent extrapolations which will be discussed in Chapter IV. Similarly, Figure 11 is a plot of Θ_Σ vs. $S = y_\Sigma/R$ for five values

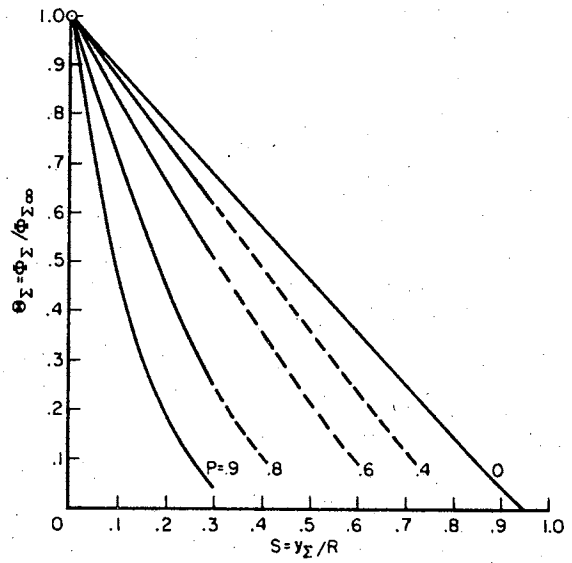

Figure 11. Conductivity correction factor as a function of the coil spacing parameter S for several radial positions of the probe.

of the parameter $P = p/R$ and extrapolations are represented by dashes. Additional points were not computed because each calculation of Θ_Σ consumed about one-half hour of the computer time. However, the data reduction method presented in Chapter IV shows that satisfactory results can be achieved with the curves of Figures 10 and 11.

Tabular values, correct to three significant figures, are listed for convenience in Table II.

TABLE II

CONDUCTIVITY CORRECTION FACTORS

P = p/R	S = y_Σ/R						
	0.05	0.10	0.20	0.30	0.80	0.93	1.00
0.00	0.948	0.892	0.783	0.675	0.140	0.012	-0.050
0.40	0.937	0.871	0.742	0.615	-----	-----	-----
0.60	0.916	0.830	0.662	0.506	-----	-----	-----
0.80	0.847	0.691	0.439	0.248	-----	-----	-----
0.90	0.713	0.471	0.176	0.044	-----	-----	-----

The conductivity formulas of Chapter II may now be modified to account for the presence of a cylindrical boundary. Specifically, Equation (31) now becomes

$$\sigma = \frac{\Phi_\Sigma}{\Theta_\Sigma(S,P)} \begin{bmatrix} \text{calibration} \\ \text{constant} \end{bmatrix}. \tag{59}$$

The last expression is still limited to the case of constant conductivity.

Product of Conductivity and Velocity or $\sigma U_{||}$

Another application of the method of images yields a $\sigma U_{||}$ stream function $\psi_{||}$ such that

$$\psi_{||} = -G_{||} z\left\{\left[\overline{x+p}^2 + y^2 + z^2\right]^{-3/2} - R^3\left[\overline{px+R^2}^2 + p^2y^2 + R^2z^2\right]^{-3/2}\right\} \quad (60)$$

where $G_{||} = \sigma U_{||} m \cos \omega t$, and the y-axis has been translated to the center of the stream as in Figure 9. Using the stream function analogy explained above, the current density vector can be derived and the result is

$$\underset{\sim}{J}_{||} = -G_{||} z\left\{\left[3R^3p^2y(\overline{px+R^2}^2 + p^2y^2 + R^2z^2)^{-5/2} - 3y(\overline{x+p}^2 + y^2 + z^2)^{-5/2}\right]\underset{\sim}{i}\right.$$

$$\left.-\left[3R^3p\,\overline{px+R^2}^2(\overline{px+R^2}^2 + p^2y^2 + R^2z^2)^{-5/2} - 3(x+p)(\overline{x+p}^2 + y^2 + z^2)^{-5/2}\right]\underset{\sim}{j}\right\}. \quad (61)$$

As was the case with $\underset{\sim}{b}_t$, $\underset{\sim}{b}_{||}$ is related to $\underset{\sim}{J}_{||}$ by the triple integral

$$\underset{\sim}{b}_{||}(x',y',z',t) = \frac{\mu}{4\pi}\int\int\int \underset{\sim}{J}_{||}(x,y,z,t) \times \underset{\sim}{\nabla} r^{-1}\, dx\, dy\, dz \quad (62)$$

where $r = (\overline{x - x'}^2 + \overline{y - y'}^2 + \overline{z - z'}^2)^{1/2}$. Because the axis of the Y coil is parallel to the y-axis, only the $\underset{\sim}{j}$ component of $\underset{\sim}{b}_{||}$ will contribute to the induced electromotive force. That component, evaluated at $(x',y',z') = (-p,-y_\Sigma,0)$ and nondimensionalized with respect to R, is

$$by_{||} = \frac{-3\mu G_{||}}{4\pi R^2}\int_{-\infty}^{\infty}\int_{-1}^{1}\int_{-\sqrt{1-Y^2}}^{\sqrt{1-Y^2}} \frac{YZ^2}{(\overline{X+P}^2 + \overline{Y+S}^2 + Z^2)^{3/2}}\left[\frac{P^2}{(\overline{PX+1}^2 + P^2Y^2 + Z^2)^{5/2}}\right.$$

$$\left. - \frac{1}{(\overline{X+P}^2 + Y^2 + Z^2)^{5/2}}\right] dX\, dY\, dZ \equiv \frac{-3\mu G_{||}}{4\pi R^2}\int_{-\infty}^{\infty}\int_{-1}^{1}\int_{-\sqrt{1-Y^2}}^{\sqrt{1-Y^2}} F_Y\, dX\, dY\, dZ \quad (63)$$

where F_Y represents the integrand.

Therefore, Faraday's law predicts that the potential Φ_Y induced at the Y coil will be

$$\Phi_Y = -\left(n_Y r_Y^2\right)\left(n_p r_p^2\right)\sigma U_{||}\,\frac{3\omega I_p \mu^2}{16R^2}\sin\omega t \int\int\int F_Y\, dX\, dY\, dZ \qquad (64)$$

and, if this expression is divided by Equation (27) to eliminate probe and coil characteristics, then the result is

$$\frac{\Phi_Y}{\Phi_{Y\infty}} \equiv \Theta_Y(S,P) = \frac{3S^2}{2\pi}\int_{-\infty}^{\infty}\int_{-1}^{1}\int_{-\sqrt{1-Y^2}}^{\sqrt{1-Y^2}} F_Y\, dX\, dY\, dZ\ . \qquad (65)$$

The correction factor Θ_Y defined by Equation (65) is similar to the conductivity correction factor Θ_Σ because, for a given probe, Θ_Y represents the ratio of the signal which would be induced in a finite cylindrical region having uniform values of σ and $U_{||}$ to the signal which would be induced in an infinite region having the same uniform values of σ and $U_{||}$. For convenience, this parameter will hereafter be referred to as the velocity correction factor even though it applies to the product $\sigma U_{||}$.

As was the case with Θ_Σ, the integrations required by Equation (65) were performed numerically on a digital computer using a program similar to that used to accomplish the integrations in Equation (58). The results are presented in Figures 12 and 13. Tabular values, correct to three significant figures, are also listed in Table III. The curves of Figure 12 indicate that if $S \leq 0.10$, then the deviation of Θ_Y from unity is negligible except at the very edge of the cylindrical stream. As anticipated, the conductivity correction factors are larger than the velocity correction factors.

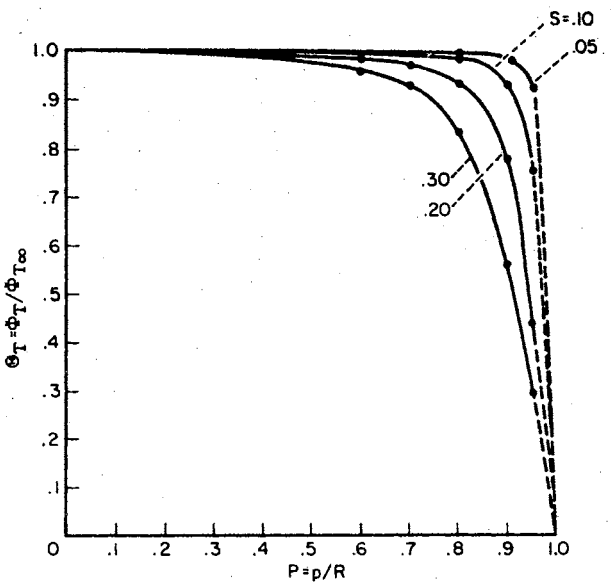

Figure 12. Correction factor for $\sigma U_{||}$ as a function of radial position of the probe for several values of the coil spacing parameter S.

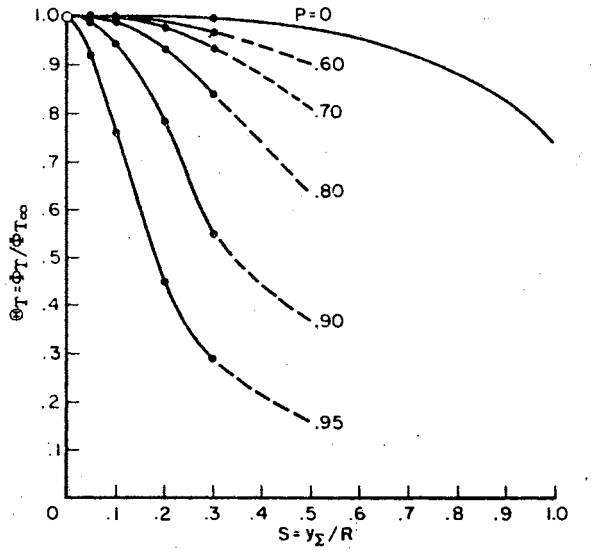

Figure 13. Correction factor for $\sigma U_{||}$ as a function of the coil spacing parameter S for several radial positions of the probe.

TABLE III

VELOCITY CORRECTION FACTORS

P = p/R	S = y_Σ/R					
	0.05	0.10	0.20	0.30	0.80	1.00
0.00	-----	-----	-----	0.994	0.880	0.731
0.60	-----	-----	0.986	0.966	-----	-----
0.70	-----	-----	0.978	0.934	-----	-----
0.80	0.997	0.988	0.937	0.839	-----	-----
0.90	0.990	0.942	0.780	0.551	-----	-----
0.95	0.925	0.754	0.443	0.291		

Equations (32) and (33) may now be modified to become

$$\sigma U_{||} = \frac{\Phi_Y}{\Theta_Y} \left[\begin{matrix} \text{calibration} \\ \text{constant} \end{matrix} \right] \tag{66}$$

and

$$U_{||} = \frac{\Phi_Y}{\Phi_\Sigma} \frac{\Theta_\Sigma}{\Theta_Y} \left[\begin{matrix} \text{calibration} \\ \text{constant} \end{matrix} \right] \tag{67}$$

Equations (66) and (67) are limited to a conducting fluid having a cylindrical boundary, uniform σ, and uniform $U_{||}$; it should be noted that the calibration constants in these two equations are not equal.

The conductivity correction factors presented in Figures 10 and 11 were verified experimentally using Probe II. (This experiment was performed with the aid of Mr. R. E. Posch.) Each of two plexiglas cylinders having different diameters was filled with an electrolyte having a conductivity of 74.8 mho/meter. Then the radial variation of the Σ coil output was recorded for each cylinder. The results were normalized

with respect to an experimentally determined value of $\Phi_{\Sigma\infty}$ to obtain Θ_Σ. Figure 14 compares the experimental values of Θ_Σ with theoretical values computed from the curves of Figure 11, and it can be seen that the differences are less than 10 percent except near the edge where the output of the Σ coil was very small and was extremely sensitive to the alinement of the probe's axis parallel to the z-axis of the cylinder.

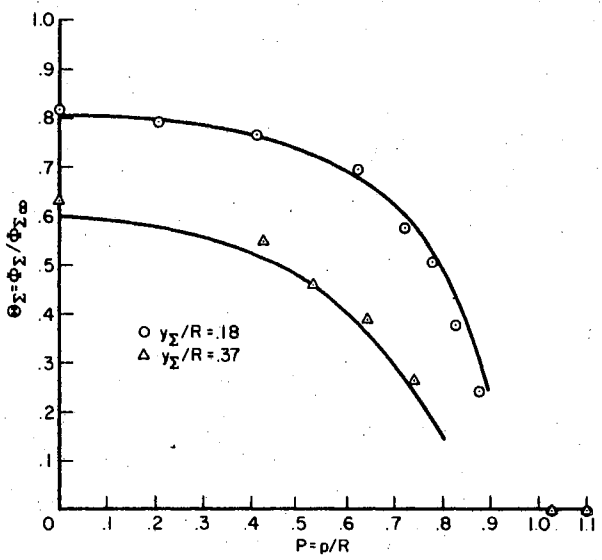

Figure 14. Comparison of numerical values of Θ_Σ (solid curves) with experimental values (points) computed from data taken with Probe II in cylinders of acid.

The probe was also placed immediately adjacent to and outside of each cylinder wall (in room air) to record the magnitude of the signal produced by the currents that were induced in the electrolyte by the primary dipole field, $\underset{\sim}{B}_p$. As indicated by the data points at $P = 1.025$ and $P = 1.10$, the result was that the signals were too small to be

observed on the oscilloscope at its maximum sensitivity setting, that is, the induced signals were at least ten times smaller than any signals obtained inside the cylinders. Now, in a free plasma jet it is reasonable to assume that the conductivity increases from zero at the edge to a maximum at the centerline. The result of the experiment indicates that, when the probe is swept through the jet, the signal induced on the Σ coil at a given radial position, say p_o, is not significantly influenced by the increased conductivity in the region $0 \leq \rho \leq p_o$ so that Φ_Σ is primarily a function of the variable conductivity in the region $p_o \leq \rho \leq R$.

CHAPTER IV

A METHOD FOR COMPUTING CONDUCTIVITY AND VELOCITY PROFILES OF AXISYMMETRIC PLASMA JETS

In this chapter a method for computing conductivity and velocity profiles is presented and applied to data taken by Probe II in a constricted-arc wind tunnel. The method is based on the premise that the continuously varying profile can be approximated by a number of steps as suggested in Figure 15. It is then assumed that each level can be treated as a cylinder of constant conductivity (or $\sigma U_{||}$) by the theory developed in Chapter III. As noted at the end of that chapter, the probe receives a negligible signal if it is outside a cylinder of conducting fluid. Hence, if the analysis of a given profile is started at the outside boundary of a jet, the calculations can proceed to the center in an explicit fashion so that all parameters are known as each step is made inward. As illustrated in Figure 15, the cylindrical plasma jet is, as a first approximation, subdivided into a finite number, n, of concentric cylindrical regions each having a different, but constant conductivity. The upper part of the sketch shows a cross section of the jet and the lower part displays a typical Φ_Σ trace together with the n-step approximation of the actual continuously-varying conductivity profile.

When the probe is located at the radial position p_1 shown in Figure 15, the second part of the previously mentioned experiment

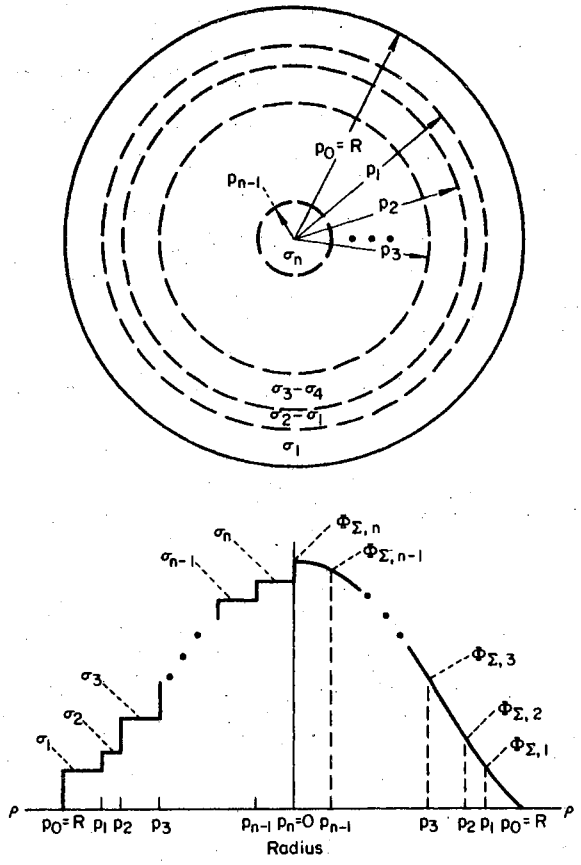

Figure 15. Method of subdividing measured profiles in order to make boundary corrections.

indicates that the influence of the increased conductivity in the inner regions has a negligible effect on the value of Φ_Σ. Therefore, $\Phi_{\Sigma,1}$ may be interpreted as the signal which results from placing the probe at a radius p_1 in a cylindrical region of radius p_o containing a fluid of conductivity σ_1. The signal $\Phi_{\Sigma,2}$ results from placing the probe simultaneously at a radius p_2 in two cylindrical regions of radii p_o and p_1 containing, respectively, fluids of conductivity σ_1 and $\sigma_2 - \sigma_1$. Similarly, $\Phi_{\Sigma,3}$ is caused by immersing the probe

simultaneously in the center of three cylindrical regions of radii p_o, p_1, and p_2 containing, respectively, fluids of conductivity σ_1, $\sigma_2 - \sigma_1$, and $\sigma_3 - \sigma_2$. The extension of this reasoning to $\Phi_{\Sigma,n}$ is straightforward and the results may be put into mathematical form by the following set of n linear equations in n unknowns:

$$\left.\begin{aligned}
\Phi_{\Sigma,1} &= \frac{\sigma_1}{C_\Sigma}\,\Theta_\Sigma\left(\frac{y_\Sigma}{p_o}\,,\,\frac{p_1}{p_o}\right)\\
\Phi_{\Sigma,2} &= \frac{\sigma_1}{C_\Sigma}\,\Theta_\Sigma\left(\frac{y_\Sigma}{p_o}\,,\,\frac{p_2}{p_o}\right) + \frac{\sigma_2 - \sigma_1}{C_\Sigma}\,\Theta_\Sigma\left(\frac{y_\Sigma}{p_1}\,,\,\frac{p_2}{p_1}\right)\\
\Phi_{\Sigma,3} &= \frac{\sigma_1}{C_\Sigma}\,\Theta_\Sigma\left(\frac{y_\Sigma}{p_o}\,,\,\frac{p_3}{p_o}\right) + \frac{\sigma_2 - \sigma_1}{C_\Sigma}\,\Theta_\Sigma\left(\frac{y_\Sigma}{p_1}\,,\,\frac{p_3}{p_1}\right) + \frac{\sigma_3 - \sigma_2}{C_\Sigma}\,\Theta_\Sigma\left(\frac{y_\Sigma}{p_2}\,,\,\frac{p_3}{p_2}\right)\\
&\;\;\vdots\\
\Phi_{\Sigma,n-1} &= \sum_{i=o}^{n-2}\left[\frac{\sigma_{i+1} - \sigma_1}{C_\Sigma}\right]\Theta_\Sigma\left(\frac{y_\Sigma}{p_i}\,,\,\frac{p_{n-1}}{p_i}\right), \qquad n \geq 2\\
\Phi_{\Sigma,n} &= \sum_{i=o}^{n-1}\left[\frac{\sigma_{i+1} - \sigma_i}{C_\Sigma}\right]\Theta_\Sigma\left(\frac{y_\Sigma}{p_i}\,,\,0\right).
\end{aligned}\right\} \tag{68}$$

In these equations C_Σ represents the probe calibration constant and σ_o is identically zero. After inserting values for Θ_Σ from Figures 10 and 11, these simultaneous equations may be solved for σ_i, $i = 1, n$.

The same technique may be applied to obtain a $\sigma U_{||}$ profile and the equations which must be solved for an n-step approximation are:

$$
\left.
\begin{aligned}
\Phi_{Y,1} &= \frac{[\sigma U_{||}]_1}{C_Y}\,\Theta_Y\left(\frac{y_\Sigma}{p_o}\,,\ \frac{p_1}{p_o}\right) \\
\Phi_{Y,2} &= \frac{[\sigma U_{||}]_1}{C_Y}\,\Theta_Y\left(\frac{y_\Sigma}{p_o}\,,\ \frac{p_2}{p_o}\right) + \frac{[\sigma U_{||}]_2 - [\sigma U_{||}]_1}{C_Y}\,\Theta_Y\left(\frac{y_\Sigma}{p_1}\,,\ \frac{p_2}{p_1}\right) \\
\Phi_{Y,3} &= \frac{[\sigma U_{||}]_1}{C_Y}\,\Theta_Y\left(\frac{y_\Sigma}{p_o}\,,\ \frac{p_3}{p_o}\right) + \frac{[\sigma U_{||}]_2 - [\sigma U_{||}]_1}{C_Y}\,\Theta_Y\left(\frac{y_\Sigma}{p_1}\,,\ \frac{p_3}{p_1}\right) \\
&\quad + \frac{[\sigma U_{||}]_3 - [\sigma U_{||}]_2}{C_Y}\,\Theta_Y\left(\frac{y_\Sigma}{p_2}\,,\ \frac{p_3}{p_2}\right) \\
&\ \ \vdots \\
\Phi_{Y,n-1} &= \sum_{i=o}^{n-2} \frac{[\sigma U_{||}]_{i+1} - [\sigma U_{||}]_i}{C_Y}\,\Theta_Y\left(\frac{y_\Sigma}{p_i}\,,\ \frac{p_{n-1}}{p_i}\right), \qquad n \geq 2 \\
\Phi_{Y,n} &= \sum_{i=o}^{n-1} \frac{[\sigma U_{||}]_{i+1} - [\sigma U_{||}]_i}{C_Y}\,\Theta_Y\left(\frac{y_\Sigma}{p_i}\,,0\right)
\end{aligned}
\right\} \qquad (69)
$$

where C_Y is the probe calibration constant, $[\sigma U_{||}]_o$ is identically zero, and the values for Θ_Y are given in Figures 12 and 13. The solutions of Equations (68) and (69) may then be combined to obtain an n-step approximation of the $U_{||}$ profile. As the number of subdivisions is increased, subject to the limitations to be discussed below, the discontinuous step profiles should approach the actual continuously varying profiles.

The data reduction technique may be divided into three parts as follows.

1. The edge of the jet may be determined from the Σ coil output provided that the response time of the probe is known. The response time of Probe II, based on a consideration of

data taken as the instrument was swept both ways through the stream, was estimated to be 0.03 second (20). Figure 16 is a

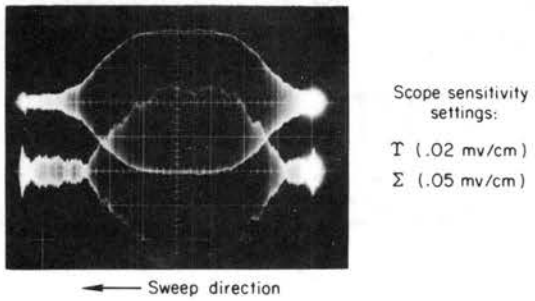

Figure 16. Data record obtained with Probe II in a constricted-arc wind tunnel having an arc current I_{arc} = 200 amp. (Courtesy of Rossow and Posch)

typical data record obtained by Rossow and Posch with Probe II and the conductivity data (lower trace) indicates that the extreme radius of the jet was about 9.5 cm. To assess the sensitivity of the data reduction method to the magnitude of the jet radius, profiles were computed for three radii: 9.0 cm, 9.5 cm, and 10.0 cm; the corrected centerline values of σ and $U_{||}$ for the three cases did not differ by more than 10 percent. Therefore, the method is not highly dependent on an accurate determination of the jet radius.

2. The null signal should be added to the Φ_Σ trace and subtracted from the Φ_Y trace; reasons for this procedure are discussed below. Then, peak-to-peak values of Φ_Σ and Φ_Y may

be plotted vs. radial position of the instrument; the radial position should be adjusted to compensate for the response time of the system. A mean value for the Φ_Y curve is used, thereby eliminating the local signal excursions caused by random stream noise.

3. The next step is to subdivide the cylindrical jet into subregions as suggested by Figure 15 and to apply Equations (68) and (69) to the Φ_Σ and Φ_Y data. It is suggested that this step be repeated several times in order to see the effect on accuracy; that is, as a first approximation, use three subregions to obtain three-step σ and $U_{||}$ profiles. Then, as a second approximation, use four subregions for the computation. Additional approximations obtained by increasing the number of subdivisions can be carried out to increase the accuracy and definition of the curves. A limitation on the maximum number of subdivisions is discussed below.

The velocity trace of Figure 16 indicates a minimum signal at about 2.8 cm from the center of the oscilloscope screen. This phenomenon is due to the fact that $\underset{\sim}{b}_{||}$ and $\underset{\sim}{B}_p$ are 180° out of phase as indicated by Equations (19) and (21). Outside the stream Φ_Y is nonzero due to the fact that the actual $\underset{\sim}{B}_p$ differs slightly from the theoretical $\underset{\sim}{B}_p$. As the probe nears the edge of the stream, the magnitude of $\underset{\sim}{b}_{||}$ increases and causes Φ_Y, which is proportional to $\underset{\sim}{B}_p + \underset{\sim}{b}_{||}$, to decrease because of the 180° phase difference. Shortly thereafter, the magnitude of $\underset{\sim}{b}_{||}$ dominates and Φ_Y begins to increase. Therefore, when the data is reduced, the Φ_Y ordinates

should be increased by the value of the null signal while the Φ_Σ ordinates should be decreased by the value of the null signal.

Using the data of Figure 16, the profiles of Figure 17 were computed for two different sets of four subregions. The corresponding profiles did not differ significantly and agreed to within 5 percent at the centerline. The dashed curves in the figure represent profiles which were not corrected for the presence of a cylindrical boundary and are based on the application of equations of the form

$$\frac{\sigma}{\Phi_\Sigma} = \left[\begin{matrix}\text{calibration} \\ \text{constant}\end{matrix}\right]_\Sigma \quad \text{and} \quad \frac{\sigma U_{||}}{\Phi_Y} = \left[\begin{matrix}\text{calibration} \\ \text{constant}\end{matrix}\right]_Y$$

to centerline values of Φ_Σ and Φ_Y. The uncorrected $U_{||}$ profile was obtained by dividing the dashed ordinates of the $\sigma U_{||}$ profile by the dashed ordinates of the σ profile. It was found that the corrected $U_{||}$ profile is in agreement with the calculations of Stine et al. (18). As anticipated, the conductivity correction factor Θ_Σ had greater influence on the reduction of data than did the velocity correction factor Θ_Y. In fact, the example presented in Figure 17 indicates that the corrections of the $\sigma U_{||}$ profile are almost negligible. However, due to the conductivity corrections, the corrected $U_{||}$ profile may differ considerably from the uncorrected $U_{||}$ profile.

As mentioned above, the choice of subregions is not completely arbitrary and it was found that the values of y_Σ and R impose two important restrictions which must be observed during the reduction of the data. The first restriction may be understood by considering the curves of Figure 18. Consider a fluid having a cylindrical boundary and, for example, a constant conductivity of 888 mho/meter. Suppose

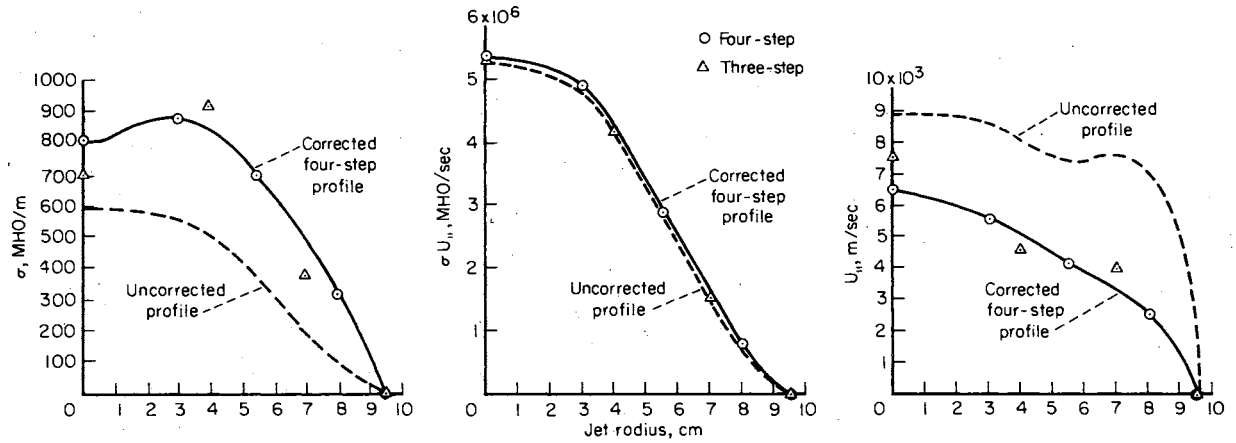

Figure 17. Conductivity and velocity profiles based on the data of Figure 16 using Probe II in a free argon plasma jet.

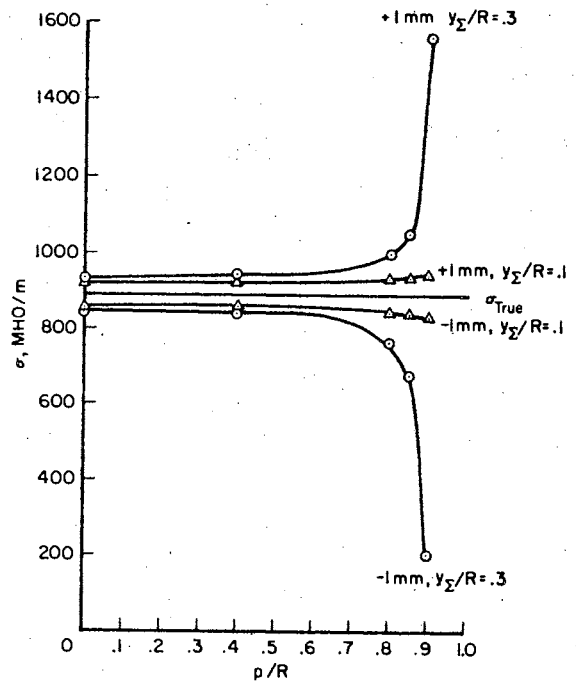

Figure 18. Uncertainty resulting from an oscilloscope reading which is in error by 1 mm.

that an oscilloscope recording is made of Φ_Σ vs. radial position, p, for this fluid. Then, if the correct Φ_Σ values are substituted into the formula

$$\frac{\sigma}{\Phi_\Sigma} = \frac{\left[\begin{matrix}\text{calibration} \\ \text{constant}\end{matrix}\right]}{\Theta_\Sigma(y_\Sigma/R, p/R)} \tag{70}$$

for different values of p, the horizontal curve marked σ_{true} will be the result. However, the smallest screen division for many oscilloscope is 0.2 cm and with the presence of a slight amount of noise, it is possible to err by as much as 0.1 cm when reading the oscilloscope data

record. Therefore, using a scope sensitivity setting of 0.05 mV/cm the calibration constant for Probe II, and the aboce equation, the error curves of Figure 18 were computed for two different values of the parameter y_Σ/R. The figure shows that a reading error of 0.1 cm can result in a large error in σ when $y_\Sigma/R = 0.3$ and $p/R \geq 0.80$. The error is not as large when $y_\Sigma/R = 0.10$.

Thus if y_Σ/R is small, the stream can be subdivided into several subregions without risking the introduction of a large oscilloscope reading error. The σ profile of Figure 19 furnishes an illustration of

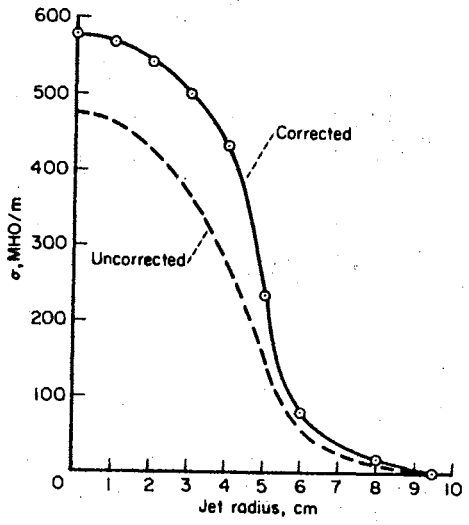

Figure 19. Conductivity profile based on data taken with Probe III by Rossow and Posch in an argon plasma jet.

this principle. The corrected σ profile, using data taken with Probe III ($y_\Sigma/R = 0.084$), was computed on the basis of nine subregions. However, the corrected σ profile of Figure 17, using data from Probe II ($y_\Sigma/R = 0.234$), is based on four subregions because it was found that further subdivision introduced large errors. It is also interesting, but not surprising, to note that the smaller the value of y_Σ/R, the smaller the resulting corrections.

The other restriction concerns the choice of the radius, p_n, of the innermost subregion. It is obvious that p_n must be chosen so that $p_n \geq y_\Sigma$. However, referring to the curve for $P = 0$ in Figure 11, it is recommended that p_n be chosen so that $p_n \geq 1.14 y_\Sigma$. This restriction on the choice of p_n places a lower limit of approximately 0.10 on the correction factor Θ_Σ. Smaller values of this factor would magnify oscilloscope reading errors by an intolerable amount.

It is difficult to estimate the overall accuracy of the preceding data-reduction technique. The uncertainty resulting from the presence of random electromagnetic noise and/or oscilloscope reading error has already been discussed. Another possible error source is the neglect of axial variations in σ and $U_{||}$. However, the magnitude of such an error is probably small because the magnitudes of the induced current vectors, $\underset{\sim}{J}_t$ and $\underset{\sim}{J}_{||}$, decrease rapidly in the axial direction and because the effects of the higher upstream values of σ and $U_{||}$ may be canceled by the lower downstream values. If the plasma stream is steady and fairly free from random electromagnetic noise, the data reduction technique presented in this chapter probably yields centerline values which differ from the true values by no more than 10 percent.

An experiment was carried out with H_2SO_4 acid solutions in plexiglas cylinders to find out how accurately the theory could predict the conductivity potential. The test was performed in the three concentric plexiglas cylinders which are sketched in the plan view of Figure 20; the centerline position of the instrument is also shown such that the axis of the probe is parallel to the z-axis of the cylinders. The depth of each cylinder was at least 18 cm because tests indicated that this value simulated a cylinder of infinite extent. All plexiglas walls were 4.7 mm thick and the inside radii of the cylinders were 5.95 cm, 9.77 cm, and 12.3 cm as indicated in Figure 20. The center cylinder was filled with a sulphuric acid solution having a conductivity of 74.8 mho/meter as determined by a conductivity cell measurement. Similarly, the two annular spaces were filled with acid solutions having conductivities of 49 and 29 mho/meter.

It was found that the probe reading at the center of the three containers could be predicted from the theory of Chapter III by considering the probe to be immersed simultaneously at the center of three cylinders of radii 12.3 cm, 9.77 cm, and 5.95 cm containing electrolytes of conductivity 29, 20, and 25.8 mho/meter, respectively. Then Equation (59),

$$\frac{\sigma}{\Phi_\Sigma} = \frac{1585}{\Theta_\Sigma(S,P)} \text{ mho/m-mV} , \tag{71}$$

may be used to compute the contribution of the currents induced in each cylinder to the total probe output. The calibration constant of 1585 given above differs from the value of 3000 given in Reference 20 because of a subsequent change in the electrical circuit. Using the correction

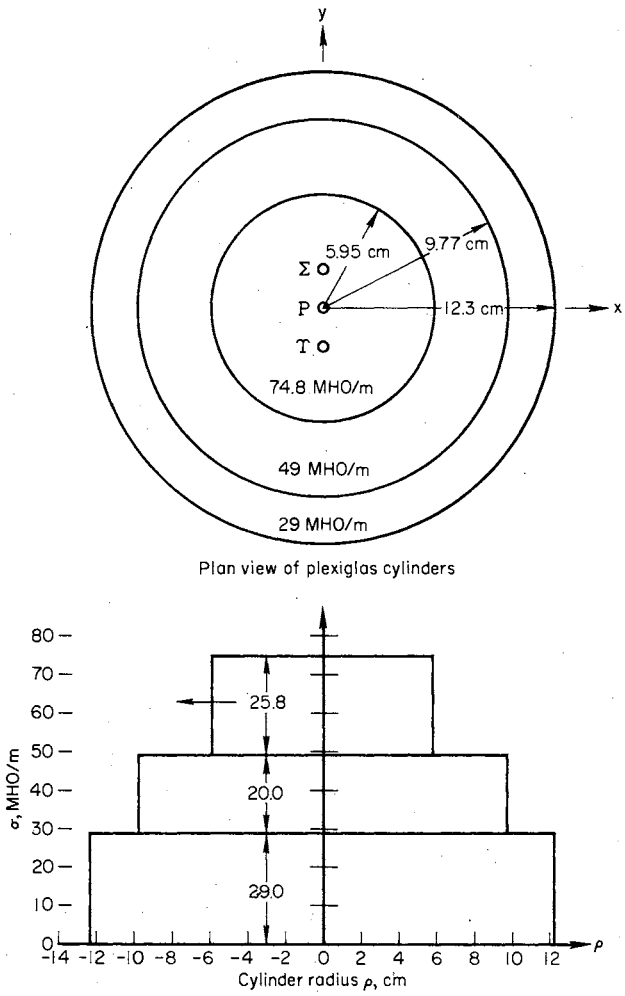

Figure 20. Conductivity measurements using Probe II (y_{Σ} = 2.22 cm) in concentric cylinders of sulphuric acid solutions.

factors of Chapter III and setting $y_\Sigma = 2.22$ cm, the predicted probe output becomes

$$\left.\begin{aligned}\Phi_\Sigma &= \frac{1}{1585}\left[29\Phi_\Sigma\left(\frac{2.22}{12.3}\,,\,0\right) + 20\Phi_\Sigma\left(\frac{2.22}{9.77}\,,\,0\right) + 25.8\Phi_\Sigma\left(\frac{2.22}{5.95}\,,\,0\right)\right] \\ &= \frac{1}{1585}\left[29 \times 0.805 + 20 \times 0.753 + 25.8 \times 0.602\right] \\ &= 0.0338 \text{ mV.}\end{aligned}\right\} \quad (72)$$

This theoretical value agrees quite well with the experimental value of 0.034 mV. The off-axis experimental values of Φ_Σ for the case $\rho \neq 0$ could not be predicted by the theory because the two inner plexiglas walls created rather complicated boundary conditions.

As mentioned in Chapter II, data in the constricted arc were obtained with three probes. The uncorrected data for the three probes did not agree as well as desired, and it was found that when the boundary corrections were made, the disagreement was increased. No difficulty was encountered with reducing the data but it was not possible to determine why the corrected probe data disagreed by as much as 40 percent on certain runs. Some of the disagreement between the probes is felt to be due to the large diameter of the coil in the case of Probe I and by the close coil spacing in the case of Probe III. Apparently, the design parameter, $2\rho_o/y_\Sigma$, is also a measure of the magnitude of mutual flow disturbance effects between support rods and coils. The values of this parameter for Probes I, II, and III were 0.291, 0.091, and 0.250, respectively. Unfortunately, both Probes I and III developed shorts in the coils during the tests so that a series of tests aimed at resolving these discrepancies could not be made. (Suggestions as to further

studies in regard to these problems are discussed in Chapter V.) Probe II survived many tests without any apparent deterioration of its performance. It is believed that this instrument was the most accurate of the three probes because it had the most favorable value of coil diameter/coil spacing (0.091) and because the velocity profile of Figure 17 compared favorably with estimates made by other means (18).

CHAPTER V

CONCLUDING REMARKS

Tests in concentric cylinders filled with acid solutions furnished reasonable confirmation of the conductivity correction factors which were used to correct the raw conductivity data for the existence of a boundary and for cross-stream σ variations. Using $\sigma U_{||}$ correction factors, the method was extended to raw $\sigma U_{||}$ data and the corrected σ and $\sigma U_{||}$ profiles were used to compute a velocity profile which agreed with other estimates.

Although these results indicate that the present design has the advantages of practicality and theoretical justification, some additional development is needed. Specifically, the following items should be investigated.

1. A suitable experimental method should be found for determining the $\sigma U_{||}$ calibration constant.
2. In an effort to ascertain the effect of the parameter $2\rho_o/y_\Sigma$ on probe performance, a smaller device which permits variation of the coil spacing should be constructed and tested for several values of $2\rho_o/y_\Sigma$ under identical conditions and the corrected data from these tests should be analyzed for the possible existence of mutual flow disturbance effects between support rods and coils.

3. Another parameter which should receive attention is the frequency, ω, of the impressed power. An oscillator having several output frequencies could be used with the probe to evaluate the importance of ω.
4. Improvement of the response time of the instrument system should be attempted.
5. Although ceramic tubing was found to be satisfactory for coil support rods, other materials, such as precision quartz tubing, should be tested.

BIBLIOGRAPHY

(1) Lin, S. C., Resler, E. L., and Kantrowitz, Arthur. "Electrical Conductivity of Highly Ionized Argon Gases Produced by Shock Waves." J. Appl. Phys. Vol. 26, No. 1. (1955) 95-109.

(2) Persson, K. B. "A Method for Measuring the Conductivity in a High Electron Density Plasma." J. Appl. Phys. Vol. 32, No. 12. (1961) 2631-2640.

(3) Koritz, H. E. and Keck, J. C. "Technique for Measuring the Electrical Conductivity of Wakes of Projectiles at Hypersonic Speeds." Rev. Sci. Instr. Vol. 35, No. 2. (1964) 201-208.

(4) Olson, R. A. and Lary, E. C. "Electrodeless Plasma Conductivity Probe Apparatus." Rev. Sci. Instr. Vol. 33, No. 12. (1962) 1350-1353.

(5) Stubbe, E. J. "A Measurement of the Electrical Conductivity of Plasmas." AIAA Preprint 66-181. Plasmadynamics Conference, Monterey, California. March 2-4, 1966.

(6) Blackman, V. H. "Magnetohydrodynamic Flow Experiment of a Steady State Nature." ARS Preprint 1007-59. (1959).

(7) Donskoi, K. V., Dunaev, Yu. A., and Prokof'ev, I. A. "Measurement of Electrical Conductivity in Gas Streams." Soviet Phys. - Tech. Phys. Vol. 7. (1963) 805-807.

(8) Akimov, A. V. and Konenko, O. R. "Measurement of Plasma Conductivity by a Radio-Frequency Method." Soviet Phys. - Tech. Phys. Vol. 10. (1966) 1126-1127.

(9) Tanaka, Hiroshi and Hagi, Mikiko. "A Method of Measurement of Plasma Conductivity. II. Example of Measurement." Japanese J. Appl. Phys. Vol. 3. (1964) 338-341.

(10) Savic, P. and Boult, G. T. "A Frequency Modulation Circuit for the Measurement of Gas Conductivity and Boundary Layer Thickness in a Shock Tube." J. Sci. Instr. Vol. 39. (1962) 258-266.

(11) Luther, Alan H. "A Non-Uniform-Plasma, Electrical Conductivity Probe." U.S. Naval Ordnance Laboratory TR 63-165. (1963).

(12) Fuhs, A. E. "An Instrument to Measure Velocity-Electrical Conductivity of Arc Plasmajets." AIAA J. Vol. 2. (1964) 667-673.

(13) Poberezhskii, L. P. "Measurement of Electrical Conductivity of Gas Jets." Soviet Phys. - Tech. Phys. Vol. 8. (1964) 1092-1094.

(14) Poberezhskii, L. P. "Measurement of Velocity and Electrical Conductivity of an Ionized Gas Stream." Soviet Phys. - Tech. Phys. Vol. 8. (1964) 1088-1092.

(15) Hollister, Donald D. "A Technique for the Experimental Determination of the Electrical Conductivity of Plasmas." AIAA J. Vol. 2, No. 9. (1964) 1568-1571.

(16) Barkan, P. and Whitman, A. M. "A Means for the Study of the Stagnation Pressure Distribution in a Current-Carrying Plasma." AIAA Preprint 66-179. (1966).

(17) Carter, A. F., McFarland, D. R., Weaver, W. R., Park, S. K., and Wood. G. P. "Operating Characteristics, Velocity and Pitot Distribution and Material Evaluation Tests in the Langley One-In.-Square Plasma Accelerator." AIAA Preprint 66-180. (1966).

(18) Stine, H. A., Watson, V. R., and Shepard, C. E. "Effect of Axial Flow on the Behavior of the Wall-Constricted Arc." NASA TM X-54,065 (1964).

(19) Gottschlich, Chad F., Enright, John A. and Cadek, F. C. "Measurement of the Velocity Distribution in a Plasmajet." AIAA J. Vol. 4. (1966) 1085-1087.

(20) Rossow, V. J. and Posch, R. E. "Coil Systems for Measuring Conductivity and Velocity of Plasma Streams." Rev. Sci. Instr. Vol. 37, No. 9. (1966) 1232-1242.

(21) Rossow, V. J. "On Series Expansions in Magnetic Reynolds Number." NASA TN D-10. (1959).

(22) Stratton, J. A. Electromagnetic Theory. McGraw-Hill, New York, N. Y. (1941).

(23) Jackson, J. D. Classical Electrodynamics. John Wiley and Sons, Inc., New York, N. Y. (1962).

(24) Delcroix, J. L. Introduction to the Theory of Ionized Gases. Interscience Publishers Inc., New York, N. Y. (1959).

(25) Chapman, S. and Cowling, T. G. The Mathematical Theory of Non-Uniform Gases, 2nd ed. Cambridge University Press, London, England. (1952).

(26) Ahtye, Warren F. "A Critical Evaluation of Methods for Calculating Transport Coefficients of Partially and Fully Ionized Gases." NASA TN D-2611. (1965).

(27) McDaniel, E. W. Collision Phenomena in Ionized Gases. John Wiley and Sons, Inc., New York, N. Y. (1964).

(28) Spitzer, Lyman, Jr. Physics of Fully Ionized Gases, 2nd ed. Interscience Publishers, Inc., New York, N. Y. (1962).

(29) Sutton, G. W. and Sherman, Arthur. Engineering Magnetohydrodynamics. McGraw-Hill, New York, N. Y. (1965).

(30) Frost, L. S. "Conductivity of Seeded Atmospheric Pressure Plasmas." J. Appl. Phys. Vol. 32, No. 10. (1961) 2029-2036.

(31) Schweitzer, S. and Mitchner, M. "Electrical Conductivity of Partially Ionized Gases." AIAA J. Vol. 4, No. 6. (1966) 1012-1019.

(32) Haworth, D. R. "Development of a Plasma Facility and Spectrographic Determination of Plasma Temperatures." Ph.D. Dissertation, Oklahoma State University, 1961.

(33) Hildebrand, F. B. Introduction to Numerical Analysis. McGraw-Hill, New York, N. Y. (1956) 319.

(34) Cambel, A. B. Plasma Physics and Magnetofluidmechanics. McGraw-Hill, New York, N. Y. (1963) 65.

(35) Thompson, W. B. An Introduction to Plasma Physics. Addison-Wesley, Palo Alto, California. (1962) 152.

(36) Handbook of Chemistry and Physics. The Chemical Rubber Co., Cleveland, Ohio. (1962) 2691.

APPENDIX A

ELECTRICAL CONDUCTIVITY FORMULAS

This section is devoted to a discussion of formulas which express electrical conductivity σ as a function of other plasma properties such as electron number density, n_e, temperature T, and average electron collision frequency $\bar{\nu}_e$. Thus, by means of these formulas, knowledge of certain plasma properties may be used to check experimental conductivity values. Conversely, experimental conductivity values may be used in conjunction with the formulas to predict certain plasma properties.

A plasma was described in Chapter I as an extremely complex mixture of charged particles, neutrals, and photons. This complexity necessitates the adoption of several restrictions, approximations, and assumptions before it is possible to derive a mathematical expression for electrical conductivity. Hence, this discussion will be restricted to ternary, neutral plasmas consisting of electrons, singly ionized positive ions, and neutral atoms; the subscripts for these three components will be e, I, and A, respectively. Furthermore, it is assumed that applied magnetic and electric fields are small so that the distribution function for each of the components deviates only slightly from a Maxwellian distribution.

It is convenient to classify plasmas on the basis of the degree of ionization α, which is defined as

$$\alpha = n_e/(n_e + n_A) \tag{73}$$

where n_e and n_A are the electron and neutral particle densities in geometry space. A gas is said to be slightly ionized if $\alpha < 10^{-4}$, partially ionized if $10^{-4} < \alpha < 10^{-2}$, and fully ionized whenever $\alpha > 10^{-2}$. These somewhat arbitrary regimes have been suggested by Delcroix (24) and others.

Most rigorous derivations of electrical conductivity expressions depend on the solutions of two integro-differential equations known as the Boltzmann equation and the Fokker-Planck equation. The dependent variable in these equations is a distribution function for each of the gas components. Hence, for a ternary plasma it is necessary to seek simultaneous solutions to three nonlinear coupled integro-differential equations.

Both the Boltzmann and the Fokker-Planck equations contain terms which express the influence of diffusion phenomenon, externally applied forces, and interparticle collisions on the distribution function. The principal difference between the two approaches lies in the collision terms: the Boltzmann equation is based on binary elastic collisions while the Fokker-Planck equation considers many long range simultaneous Coulombic interactions. Chapman and Cowling (25) present a derivation of and several solutions to the Boltzmann equation for un-ionized gases. The paper by Ahtye (26) contains a rigorous, second-order Chapman-Enskog formulation for argon and the results are valid for any value of α. However, the complexity of the rigorous solution methods necessitates the use of approximate conductivity formulas for engineering applications. Several of these formulas are presented below.

Based on a first-order solution of the Boltzmann equation and assuming that electrons are the principal charge carriers, Chapman and Cowling derived the following expression for a slightly ionized gas:

$$\sigma = \frac{3\alpha e^2}{8Q_{eA}kT}\left[\frac{kT(m_e + m_A)}{2\pi m_e m_A}\right]^{-1/2}, \text{ mho/meter} \qquad (74)$$

In this equation the elementary charge is $e = 1.602\times10^{-19}$ coulomb, Boltzmann's constant is $k = 1.3805\times10^{-23}$ joule/^{o}K, Q_{eA} is the total electron-atom collision cross section in meter^2, T is the temperature in ^{o}K, and m_e, m_A are, respectively, the electron and atomic masses in kilograms. Because $m_e/m_A \ll 1$, Equation (74) may be simplified to

$$\sigma = 1.09\times10^{-12}\frac{\alpha}{Q_{eA}T^{1/2}}, \text{ mho/meter} \qquad (75)$$

Equation (75) is restricted to a singly ionized ternary plasma such that $\alpha < 10^{-4}$. The quantity Q_{eA} is a function of temperature and the polarizability of the particular atomic species (24). Chapter 4 of McDaniel (27) contains experimental Q_{eA} values for several gases.

When $\alpha = 1$, the gas is fully ionized and, for this case, Spitzer (28) has derived a formula for σ based on a solution of the Fokker-Planck equation. This result, which considers electron and ion currents, is

$$\sigma = 1.53\times10^{-2}T^{3/2}[\ln\Lambda]^{-1} \text{ mho/meter} \qquad (76)$$

where

$$\Lambda = 11.94\times10^{-2}\left(\frac{\epsilon_o kT}{n_e^{1/2}e^2}\right)^{3/2} \qquad (77)$$

and the permittivity of free space is $\epsilon_o = (36\pi\times10^{9})^{-1}$, farad/meter.

Equation (76) assumes elastic collisions, considers only e-e and e-I collisions, and neglects close encounters which result in a particle deflection angle greater than 90^{o}. In spite of these restrictions, this formula deviates no more than 7 percent from the more exact analysis of Ahtye. Furthermore, the experimental data of Lin et al. (1) suggests that Equation (76) is valid for $10^{-2} < \alpha < 1.0$. In the derivation of Equation (76), certain nondominant terms were neglected by Spitzer so that the result is correct to terms of order $(\ln \Lambda)^{-1}$.

In Chapter 5 of Sutton and Sherman (29), the Boltzmann equation is solved for a Lorentzian gas which is defined as a binary gas such that the mass of one type of particle (electron) is very small compared with the mass of the other type (say, an atom), and where the interaction between like particles is negligible compared with the interaction between unlike particles. An approximate formula which results from this solution is

$$\sigma = n_e e^2/m_e \bar{\nu}_e \tag{78}$$

where $\bar{\nu}_e$ is the total average electron collision frequency defined by the sum

$$\bar{\nu}_e = \bar{\nu}_{eA} + \bar{\nu}_{eI} = n_A \bar{c}_e Q_{eA} + n_I \bar{c}_e Q_{eI} \tag{79}$$

and $\bar{c}_e$ is the mean thermal electron speed which is given by

$$\bar{c}_e = (8kT/\pi m_e)^{1/2}. \tag{80}$$

Values for Q_{eA} and Q_{eI} vs. $\bar{c}_e$ may be found in Chapter 4 of McDaniel. Equation (78) neglects $\bar{\nu}_{ee}$ and assumes that electrons are the principal charge carriers. If there are several species present in the ionized gas, Equation (78) may still be used by substituting for $\bar{\nu}_e$

the expression

$$\bar{\nu}_e = \sum_s (\bar{\nu}_{eA})_s + \sum_s (\bar{\nu}_{eI})_s \tag{81}$$

where s refers to a particular gas component.

For a ternary mixture, Lin et al. (1) proposed an approximation for $\bar{\nu}_{eI}$ of the form

$$\bar{\nu}_{eI} = \frac{n_e e^2}{m_e} \frac{\ln \Lambda}{1.53\times10^{-2} T^{3/2}} \tag{82}$$

so that Equation (78) will reduce to Equation (76) in the fully ionized limit. Thus, Equations (78), (79), and (82) combine to yield

$$\sigma = \frac{\alpha}{\dfrac{\alpha \ln \Lambda}{1.53\times10^{-2} T^{3/2}} + \dfrac{(1-\alpha) Q_{eA} T^{1/2}}{1.09\times10^{-12}}} \tag{83}$$

where the coefficient of Q_{eA} has been adjusted to yield Equation (75) for small α. As before, Q_{eA} may be read from the data of McDaniel.

Ahtye has examined the accuracy of Equation (83) for argon and found that the rigorous second-order Chapmann-Enskog formulation predicted values which were almost two orders of magnitude lower whenever $10^{-4} \leq \alpha \leq 10^{-3}$. Several factors may account for this discrepancy:

1. Equation (83) does not consider ion currents which may not be negligible as $\alpha \to 10^{-3}$.
2. Second-order collision coupling effects and I-I collisions are also ignored.
3. In Equation (83) the cross section Q_{eA} must, for simplicity, be evaluated at some mean value whereas, in Ahtye's analysis, Q_{eA} is an empirically determined function of the relative

thermal speed between electrons and atoms as well as the interparticle potential function. The empirical expression for Q_{eA} appears under an integral which must be evaluated to obtain $\bar{\nu}_{eA}$.

Frost (30) proposed a mixing rule for a partially ionized Lorentzian gas containing several atomic species and the rule was based on the use of a nonconstant empirical function for Q_{eA} while I-I collisions and the ion current contributions were ignored. Schweitzer and Mitchner (31) solved the Boltzmann equation by making use of the fact that $m_e/m_A \cong m_e/m_I \ll 1$ to simplify a third-order Chapman-Enskog formulation. Thermal diffusion and ion currents were not considered in this paper. Schweitzer and Mitchner also compared their results with Frost's mixing rule and found that the two agreed to better than 15 percent for all $\alpha \leq 1$.

Thus, it appears that the simple formulas of Equations (75), (76), and (83) are adequate for preliminary engineering design calculations. If greater precision is desired for α in the range $10^{-4} < \alpha < 10^{-2}$ Frost's mixing rule should be applied.

Assuming that Q_{eA} is a function of temperature only, the above conductivity formulas indicate that σ is a function of α, n_e, and T. But α, for a given gas, is a function of p and T by virtue of the Saha equation

$$\alpha = \frac{GT^{5/4}}{p^{1/2}} \exp\left(\frac{-q_1}{2kT}\right) \tag{84}$$

where G is a constant which depends on the statistical weights of the positive ion and the atom and q_1 is the first ionization potential of the gas atom. The static pressure, p, may be determined by means of

an appropriate pressure transducer, the temperature, T, may be measured by spectroscopy, and n_e may be inferred from the data of a Langmuir probe. Haworth (32) gives a detailed account of spectroscopic temperature diagnostics and Sutton and Sherman present an analysis of the Langmuir probe.

APPENDIX B

DIGITAL COMPUTER INTEGRATION USING GAUSSIAN QUADRATURE

The triple integrations required by Equations (58) and (65) of Chapter III were performed on an IBM 7090/7094 Computer System using a Fortran IV Gaussian-quadrature program. The Gaussian-quadrature method, as presented by Hildebrand (33) for the case of one independent variable, is based on the formula

$$\int_{-1}^{1} f(x)dx = \sum_{k=1}^{m} H_k f(x_k) + E \tag{85}$$

where x_i is the ith zero of the Legendre polynomial $P_m(x)$ and where

$$H_i = \frac{2}{mP_{m-1}(x_i)P'_m(x_i)} . \tag{86}$$

The error E may be written as

$$E = \frac{2^{2m+1}(m!)^4}{(2m+1)[(2m)!]^3} f^{(2m)}(\xi) \tag{87}$$

in which ξ is some point in the interval (-1, 1). If the interval of integration is not (-1, 1), then a suitable transformation may be applied to the independent variable so that the above formulas may be applied. It is assumed that the function f(x) is analytically defined and it can be shown that if f(x) is a polynomial of degree 2m-1, then E = 0. The method may be extended to any finite number of independent

variables by the use of a nested integration procedure. Gaussian quadrature yields approximately the same degree of accuracy as Lagrangian quadrature but the former is "faster" because it does not require the evaluation of as many ordinates as the latter (see page 312 of Reference 33).

Figure 21 is a copy of a typical program which was used to evaluate the triple integrals of Chapter III. This particular program was written in cylindrical coordinates for the case $P = p/R = 0$. The

```
                TC1101
      EXTERNAL FORMULA NUMBER   -   SOURCE STATEMENT

C     CONDUCTIVITY CORRECTIONS  INTEGRATE F(S,P,R,T,Z)
      DIST(R,Z)= (SQRT(R*R+Z*Z))**3
      DENOM(R,T,Z)=(SQRT(R*R+S*S-2.0*R*S*SIN(T)+(Z-.707*S)**2))**3
      UP(R,T)=R*R*(R-S*SIN(T))
      F(R,T,Z)=UP(R,T)/(DIST(R,Z)*DENOM(R,T,Z))
      DIMENSION BR(5),BT(5),BZ(5)
      NAMELIST/INPUT/S,R1,R2,T1,T2,Z1,Z2,NR,NT,NZ
   13 READ(5,INPUT)
      WRITE(6,INPUT)
      K=0
   14 K=K+1
   15 BZ(K)=GAUSS1(Z1,Z2,NZ,Z)
      BT(K)=GAUS2(T1,T2,NT,T)
      BR(K)=GAUS3(R1,R2,NR,R)
      BR(K)=F(R,T,Z)
      BT(K)=BR(K)
      BZ(K)=BT(K)
      WRITE(6,98)BZ(K)
   98 FORMAT(1HO,6HBZ(K)=,E15.8)
      NR=NR+1
      NT=NT+1
      NZ=NZ+1
      IF(2-K)20,20,14
   20 EPS=BZ(K)-BZ(K-1)
      WRITE(6,99)EPS
   99 FORMAT(1HO,4HEPS=,E15.8)
      GO TO 13
      END
```

Figure 21. Typical computer program used to accomplish the triple integrations of Equation (58).

first four statements are used to define the integrand $F(R,T,Z)$ where R is the radial coordinate, T is the azimuthal angle, and Z is the axial coordinate. The next item is an input statement using a NAMELIST subroutine to input the parameter $S(=y_\Sigma/R)$; the limits of integration: $R1 \leq R \leq R2$, $T1 \leq T \leq T2$, $Z1 \leq Z \leq Z2$; and the mesh-width parameters:

NR, NT, and NZ. An example may clarify the use of the parameters NR, NT, and NZ. If the radial limits of integration are input as R1 = 0.1 and R2 = 0.3, then an input of NR = 4 would cause the division of the interval $0.1 \leq R \leq 0.3$ into four equal subintervals over each of which the Gaussian quadrature formulas of Equations (85), (86), and (87) would be applied using a value of m = 10.

The calling statement for the 10-point Gaussian quadrature subroutine is BZ(K) = GAUSS(Z1, Z2, NZ, Z). The next two statements call subroutines for nested integration. The statement BR(K) = F(R,T,Z) causes the execution of the integration

$$BR(K) = \int_{R1}^{R2} F(R,T,Z)\,dR.$$

Then, BT(K) = BR(K) causes the computation

$$BT(K) = \int_{T1}^{T2} BR(K)\,dT\ ,$$

and the final integration,

$$BZ(K) = \int_{Z1}^{Z2} BT(K)\,dZ\ ,$$

is instigated by the statement BZ(K) = BT(K).

To check convergence of the numerical method, the integrations were repeated a second time after each of the parameters NR, NT, and NZ had been increased by unity. Convergence was considered adequate if the difference (called EPS in the program) between successive integrations was less than ±0.0005.

For the case $P \neq 0$, it was more convenient to use rectangular coordinates and the region of integration was subdivided into twenty subregions. The subdivisions were chosen so as to exclude the two

singularities and to permit the use of larger values of NR, NT, and NZ in the subregions close to the singularities. Each of the twenty subregions was further subdivided in the axial direction. Computer time reguired to evaluate the triple integral for one set of values for S and P was approximately 30 minutes. Figure 22 is a copy of a typical output for the program of Figure 21.

```
$INPUT
S      =          0.93000000E 00,
R1     =          0.80000000E 00,
R2     =          0.09999999E 01,
T1     =          0.20943999E 01,
T2     =          0.47123999E 01,
Z1     =          0.91999999E 00,
Z2     =          0.52000000E 01,
NR     =                1,
NT     =                2,
NZ     =                2,
$ END
BZ(K)= 0.31221495E-01
BZ(K)= 0.31221494E-01
EPS=-0.69849193E-09
```

Figure 22. Typical computer program output for the program of Figure 21.

In the programs which were written in rectangular coordinates, the total region of integration was subdivided in such a way that each singularity was at the center of a cubical subregion whose volume was approximately 10^{-24}. The computer was not allowed to integrate in these small subregions.

Therefore, it was necessary to perform an analytical estimate of the value of the integrations taken over a typical excluded cubical subregion. Consider the first term in the integrand of Equation (71). If the origin of the X,Y,Z system is translated to the location of the Y coil at (X,Y,Z) = (-P,-S,0), then the absolute value of the result will be

$$\left| \int_0^{10^{-8}} \int_0^{10^{-8}} \int_0^{10^{-8}} \frac{P^2 \bar{Z}^2 (\bar{Y} - S)\, d\bar{X}\, d\bar{Y}\, d\bar{Z}}{(\bar{X}^2 + \bar{Y}^2 + \bar{Z}^2)^{3/2} [(P\bar{X} + 1 - P^2)^2 + P^2(\bar{Y} - S)^2 + \bar{Z}^2]^{5/2}} \right|$$

$$\leq \left\{ \frac{P^2 |\bar{Y} - S|}{[(P\bar{X} + 1 - P^2)^2 + P^2(\bar{Y} - S)^2 + \bar{Z}^2]^{5/2}} \right\}_{\substack{\text{max.} \\ \text{value} \\ \text{on cube}}} \times$$

$$\int_0^{10^{-8}} \int_0^{10^{-8}} \int_0^{10^{-8}} \frac{\bar{Z}^2\, d\bar{X}\, d\bar{Y}\, d\bar{Z}}{(\bar{X}^2 + \bar{Y}^2 + \bar{Z}^2)^{3/2}}$$

where $X = \bar{X} - P$, $Y = \bar{Y} - S$, $Z = \bar{Z}$ and the singularity is now located at $(\bar{X},\bar{Y},\bar{Z}) = (0,0,0)$. Since $\bar{X}$, $\bar{Y}$, and $\bar{Z}$ are very small compared with S and P, the maximum value of the factor within the braces in the cubical region of integration is approximately

$$\frac{P^2 S}{[(1 - P^2)^2 + P^2 S^2]^{5/2}} .$$

Next, it is convenient to transform to spherical coordinates by setting $\bar{X} = r \sin\varphi \cos\theta$, $\bar{Y} = r \sin\varphi \sin\theta$, $\bar{Z} = r \cos\varphi$ so that

$$\int_0^{10^{-8}} \int_0^{10^{-8}} \int_0^{10^{-8}} \frac{\bar{Z}^2 \, d\bar{X} \, d\bar{Y} \, d\bar{Z}}{(\bar{X}^2+\bar{Y}^2+\bar{Z}^2)^{3/2}} \leq \int_0^{\pi} \int_0^{2\pi} \int_0^{r_1} \frac{r^4 \cos^2\varphi \sin\varphi \, dr \, d\theta \, d\varphi}{r^3}$$

$$= \frac{4\pi r_1^2}{3}$$

where r_1 is the radius of any sphere which contains the cubical sub-region. Therefore, it is now possible to write

$$\left| \int_0^{10^{-8}} \int_0^{10^{-8}} \int_0^{10^{-8}} \frac{P^2\bar{Z}^2(\bar{Y} - S) d\bar{X} \, d\bar{Y} \, d\bar{Z}}{(\bar{X}^2+\bar{Y}^2+\bar{Z}^2)^{3/2}[(P\bar{X}+1-P^2)^2 + P^2(\bar{Y}-S)^2 + Z^2]^{5/2}} \right|$$

$$\leq \frac{4\pi S P^2 r_1^2}{3[(1-P^2)^2 + P^2S^2]^{5/2}} \qquad (88)$$

The right-hand side of this expression is a maximum when the value of P is close to one and when the value of S is small. A sphere of radius $r_1 = 10^{-5}$ would certainly contain the cubical region in question and the value $S = 0.05$ probably represents the smallest practical limit of the ratio y_Σ/R. Therefore, substituting these values and setting $P = 0.95$, the right-hand side of Equation (88) is found to be of the order 10^{-5}, which is a negligible quantity compared with the smallest value for the triple integral obtained by computer integration over all regions except those containing singularities. Therefore, Equation (88) justifies the neglect of the cubic region containing the singularity $(X,Y,Z) = (-P,-S,0)$. The other three singularities contained in Equations (56) and (63) were checked in the same manner with similar results.

Although the analytical interval of integration along the Z-axis was $-\infty \leq Z \leq \infty$, it was found that the regions such that $|Z| > 6.0$ contributed a negligible amount to the value of the triple integrals.

APPENDIX C

DISPLACEMENT CURRENTS IN PLASMAS AND ELECTROLYTES

Neglect of the displacement current term, common to almost all previous conductivity probe theories, should be justified for both plasma and electrolyte. The complete form for Equation (6) is

$$\underset{\sim}{\nabla} \times \underset{\sim}{H} = \underset{\sim}{J} + \frac{\partial \underset{\sim}{D}}{\partial t} \tag{89}$$

where $\underset{\sim}{H}$ is the magnetic field intensity vector, $\underset{\sim}{J}$ is the current density vector, $\underset{\sim}{D}$ is the electric displacement vector, and $\partial\underset{\sim}{D}/\partial t$ is called the displacement current. Assuming that plasmas and electrolytes are linear, isotropic media, the constitutive equations are

$$\underset{\sim}{D} = \epsilon \underset{\sim}{E} \tag{90}$$

$$\underset{\sim}{H} = \frac{1}{\mu} \underset{\sim}{B} \tag{91}$$

where ϵ is the dielectric constant and μ, the magnetic permeability, may be taken to be $\mu = \mu_o = 4\pi \times 10^{-7}$ henry/m for plasmas and electrolytes.

By virtue of Ohm's law, $\underset{\sim}{J} = \sigma\underset{\sim}{E}$, and setting $\underset{\sim}{E} = \underset{\sim}{E}_o \cos \omega t$, Equations (89), (90), and (91) may be combined to yield

$$\underset{\sim}{\nabla} \times \frac{\underset{\sim}{B}}{\mu} = \sigma \underset{\sim}{E}_o \cos \omega t - \omega\epsilon \underset{\sim}{E}_o \sin \omega t$$

or

$$\underset{\sim}{\nabla} \times \frac{\underset{\sim}{B}}{\mu} = \underset{\sim}{E}_o \sigma \left[1 + \left(\frac{\omega\epsilon}{\sigma}\right)^2\right]^{1/2} \cos(\omega t + \alpha) \tag{92}$$

where $\alpha = \cos^{-1}[1 + (\omega\epsilon/\sigma)^2]^{1/2}$. Thus, the displacement current is negligible if $\omega\epsilon/\sigma \ll 1$.

Cambel (34) has derived a formula to evaluate the ratio $\omega\epsilon/\sigma$ for a plasma. It is given as

$$\frac{\omega\epsilon}{\sigma} = \frac{\omega}{\bar{\nu}_e}\left[\frac{\bar{\nu}_e^2}{\omega_p^2} + \left(\frac{\omega^2}{\omega_p^2} - 1\right)\right] \tag{93}$$

where ω is the impressed frequency, $\bar{\nu}_e$ is the total electron collision frequency, and ω_p is the plasma electron frequency defined in Equation (2). Substitution of typical gas discharge values of $\bar{\nu}_e = 1.2\times10^9$ sec^{-1} and $\omega_p = 5.6\times10^{11}$ sec^{-1} from page 11 of Thompson (35) reduces Equation (92) to the approximate formula

$$\frac{\omega\epsilon}{\sigma} \cong \frac{\omega}{1.2\times10^9}$$

The design of Rossow and Posch uses a 100-kHz power supply so that $\omega\epsilon/\sigma \cong 1/1910$. However, ω for the probes inspired by Blackman's instrument is approximately 23 MHz for which $\omega\epsilon/\sigma \cong 1/8.3$. Therefore, neglect of $\partial\underset{\sim}{D}/\partial t$ in a plasma seems justifiable for the former but may be questionable for the latter.

For electrolytes, the ratio $\omega\epsilon/\sigma$ can be evaluated from handbook (36) values for σ and ϵ. Assuming a standard solution of sulphuric acid and water having a conductivity of 77.7 mho/meter at 21° C and a dielectric constant equal to that of pure water, the ratio becomes

$$\frac{\omega\epsilon}{\sigma} = 0.91\times10^{-11}\omega \tag{94}$$

Therefore, for $\omega = 2\pi\times10^5$ as used by Rossow and Posch,

$$\frac{\omega\epsilon}{\sigma} = 5.71\times10^{-6}$$

and for $\omega = 46\pi \times 10^6$ as used by Blackman,

$$\frac{\omega\epsilon}{\sigma} = 1.32 \times 10^{-3}.$$

Hence, it appears that $\partial \underset{\sim}{D}/\partial t$ is negligible at both frequencies in the H_2SO_4 electrolyte.

VITA

Edward William Vendell

Candidate for the Degree of

Doctor of Philosophy

Thesis: BOUNDARY CORRECTIONS FOR A THREE-COIL CONDUCTIVITY/VELOCITY PLASMA PROBE

Major Field: Mechanical Engineering

Biographical:

Personal Data: Born in Ogden, Utah, August 11, 1932, the son of Edward William and Mary Alice Vendell.

Education: Attended Weber State College, Ogden, Utah; received the Bachelor of Science degree from the University of Utah, Salt Lake City, Tuah, with a major in Mechanical Engineering, in August 1955; received the Master of Science degree from the University of Utah, Salt Lake City, Utah, with a major in Mathematics, in August 1960; completed requirements for the Doctor of Philosophy degree in May 1967.

Professional Experience: Refrigeration Engineer with the American Blower Corporation, Detroit, Michigan, from August 1955 to June 1957; Propulsion Engineer with the Martin Company, Denver, Colorado, from June 1957 to September 1958; Graduate Teaching Assistant in Mathematics at the University of Utah, Salt Lake City, Utah from September 1958 to June 1960; Assistant Professor of Mechanical Engineering at Utah State University, Logan, Utah from June 1960 to May 1967.

Professional Organizations: The author is a member of the following honorary, educational, and professional

organizations: Pi Tau Sigma, American Society for Engineering Education, American Society of Mechanical Engineers, and the American Institute of Aeronautics and Astronautics.